On the relative bias of void tracers in the Dark Energy Survey

G. Pollina[1,2★], N. Hamaus[2], K. Paech[1,2], K. Dolag[2,3], J. Weller[1,4,2], C. Sánchez[5,6], E. S. Rykoff[7,8],
B. Jain[5], T. M. C. Abbott[9], S. Allam[10], S. Avila[11], R. A. Bernstein[12], E. Bertin[13,14],
D. Brooks[15], D. L. Burke[7,8], A. Carnero Rosell[16,17], M. Carrasco Kind[18,19], J. Carretero[6],
C. E. Cunha[7], C. B. D'Andrea[5], L. N. da Costa[16,17], J. De Vicente[20], D. L. DePoy[21], S. Desai[22],
H. T. Diehl[10], P. Doel[15], A. E. Evrard[23,24], B. Flaugher[10], P. Fosalba[25,26], J. Frieman[10,27], J. García-
Bellido[28], D. W. Gerdes[23,24], T. Giannantonio[29,30,2], D. Gruen[7,8], J. Gschwend[16,17], G. Gutierrez[10],
W. G. Hartley[15,31], D. L. Hollowood[32], K. Honscheid[33,34], B. Hoyle[4,2], D. J. James[35], T. Jeltema[32],
K. Kuehn[36], N. Kuropatkin[10], M. Lima[37,16], M. March[5], J. L. Marshall[21], P. Melchior[38], F. Menanteau[18,19],
R. Miquel[39,6], A. A. Plazas[40], A. K. Romer[41], E. Sanchez[20], V. Scarpine[10], R. Schindler[8], M. Schubnell[24],
I. Sevilla-Noarbe[20], M. Smith[42], M. Soares-Santos[43], F. Sobreira[44,16], E. Suchyta[45], G. Tarle[24],
A. R. Walker[9], W. Wester[10]

(DES Collaboration)

Author affiliations are listed at the end of this paper

ABSTRACT

Luminous tracers of large-scale structure are not entirely representative of the distribution of mass in our Universe. As they arise from the highest peaks in the matter density field, the spatial distribution of luminous objects is biased towards those peaks. On large scales, where density fluctuations are mild, this bias simply amounts to a constant offset in the clustering amplitude of the tracer, known as linear bias. In this work we focus on the *relative* bias between galaxies and galaxy clusters that are located inside and in the vicinity of cosmic voids, extended regions of relatively low density in the large-scale structure of the Universe. With the help of hydro-dynamical simulations we verify that the relation between galaxy and cluster overdensity around voids remains linear. Hence, the void-centric density profiles of different tracers can be linked by a single multiplicative constant. This amounts to the same value as the relative linear bias between tracers for the largest voids in the sample. For voids of small sizes, which typically arise in higher density regions, this constant has a higher value, possibly showing an environmental dependence similar to that observed for the linear bias itself. We confirm our findings by analysing mocks and data obtained during the first year of observations by the Dark Energy Survey. As a side product, we present the first catalogue of three-dimensional voids extracted from a photometric survey with a controlled photo-z uncertainty. Our results will be relevant in forthcoming analyses that attempt to use voids as cosmological probes.

Key words: Cosmology: observations – large-scale structure of Universe – galaxies: clusters: general

1 INTRODUCTION

Most of the mass content in our Universe is composed of cold dark matter (CDM), currently described as a non-relativistic collisionless fluid which is responsible for the formation of halos, gravitationally bound clumps of dark matter that provide the potential wells in which baryons can cool and collapse to give birth to the galaxies we observe in the sky (Peebles 1980). While the quest for the nature of dark matter remains unresolved, currently the only way to infer its properties is indirect, via the gravitational interaction it exerts on the luminous constituents of the cosmos. To map the CDM one can therefore rely on the distribution of luminous tracers, such as galaxies and clusters of galaxies. Unfortunately, these objects are located only in the highest peaks of the underly-

★ gpollina@usm.lmu.de

ing matter density field, therefore their clustering properties do not exactly mirror those of the CDM: galaxies and clusters of galaxies are biased tracers of the total mass distribution (Kaiser 1984). On small scales, where highly non-linear effects are important, this bias constitutes an unknown function of space and time. But on large scales, where density fluctuations remain within the linear regime, it can be modelled as a multiplicative offset in the clustering amplitude. The latter is known as *linear bias* and depends on a number of properties of the tracer population, one of the most important being the mass of its host halos: tracers residing in more massive halos exhibit a higher clustering bias (for a comprehensive review, see Desjacques et al. 2016).

Typically, bias has been studied via the correlation function or the power spectrum of all tracers as a whole, regardless of their cosmic-web environment (see, e.g., Smith et al. 2007; Cacciato et al. 2012; Springel et al. 2018; Simon & Hilbert 2017; Dvornik et al. 2018, and references therein). In a recent paper, however, Pollina et al. (2017) investigated the properties of bias focusing on tracers located in the vicinity of cosmic voids, large and relatively empty regions of large-scale structure. Voids, amongst all other structure types, are the largest in the Universe and make up the dominant fraction of its space. In Pollina et al. (2017) simulations were analysed to determine the absolute clustering bias of various tracers with respect to the total mass distribution. In order to mimic an observational approach, voids were identified in the distribution of tracers to define void catalogues. Then, both the density of dark matter particles and the density of the tracers themselves was investigated as a function the distance r to the centers of these voids. In particular, it was found that the void-tracer cross-correlation function $\xi_{\mathrm{vt}}(r)$ exhibits a linear relation with the corresponding void-matter cross-correlation function $\xi_{\mathrm{vm}}(r)$, with a proportionality constant b_{slope},

$$\xi_{\mathrm{vt}}(r) = b_{\mathrm{slope}} \, \xi_{\mathrm{vm}}(r). \qquad (1)$$

Furthermore, Pollina et al. (2017) investigated the dependence of b_{slope} on void size. It was found that the best-fit value for b_{slope} decreases monotonically towards larger voids, and saturates to a constant number for the largest voids. This number was shown to coincide with the linear tracer bias b_{t}, which can be either calculated from theory, or determined using the common bias estimators. Hence, b_{slope} in Equation (1) can be expressed as follows:

$$b_{\mathrm{slope}}(r_{\mathrm{v}}) \begin{cases} > b_{\mathrm{t}} \text{ , for } r_{\mathrm{v}} < r_{\mathrm{v}}^{+} \\ = b_{\mathrm{t}} \text{ , for } r_{\mathrm{v}} \geqslant r_{\mathrm{v}}^{+} \text{ ,} \end{cases} \qquad (2)$$

where r_{v} is the average, and r_{v}^{+} the critical effective void radius of the sample. In other words, Equation (1) linearly relates tracer and matter densities around voids in all cases, but b_{slope} coincides with the linear bias b_{t} only when voids of size $r_{\mathrm{v}} > r_{\mathrm{v}}^{+}$ are considered in the measurement (for visualization please refer to Fig. 4 of Pollina et al. 2017). The precise value of r_{v}^{+} depends on various properties of the tracer distribution itself, such as its sparsity and bias. Nevertheless, Equation (1) provides a very simple guideline of how to infer the distribution of mass around voids in the tracer distribution[1]. The aim of this paper is to show that the same applies when relating different types of tracers around voids, both in simulations, and for the first time in observational data as well.

The importance of the result summarized in the previous paragraph can be better understood if we consider how building a coherent framework within void-cosmology has been so far a very complicated task. For example, obtaining accurate predictions on the most basic statistic, the void number counts, has always been particularly difficult. This has to do with the fact that the definition criteria for voids and their associated assumptions are not unique and typically differ between theory and practice. It is generally agreed that voids are vast regions of large-scale structure with a density below the average density of the Universe. However, due to the multi-scale nature of cosmic web, it is unclear how to divide local underdensities of different shape with multiple levels of nested substructure into a unique set of distinct objects. In a pioneering theoretical study, Sheth & van de Weygaert (2004) define voids as spherically symmetric underdensities that undergo shell crossing at their boundaries. Their initial density profile is assumed to have an inverted top-hat form, and spherical evolution is adopted to predict the final void abundance following the excursion-set formalism (also see Jennings et al. 2013; Nadathur & Hotchkiss 2015; Falck & Neyrinck 2015; Chan et al. 2014). In practice, however, these assumptions are hardly ever justified. Two general directions have been pursued to overcome this problem. One is to modify or relax specific assumptions in the theory of Sheth & van de Weygaert (2004), such as demanding volume conservation for the entire void sample (Jennings et al. 2013), or allowing the critical density threshold for void formation to vary as a free parameter (Pisani et al. 2015). The other option is a modification of void catalogues via selection cuts, which guarantee the assumptions in Sheth & van de Weygaert (2004) to be satisfied (Ronconi & Marulli 2017). Both approaches show promising results and will likely play a role in future analyses that attempt to extract cosmological signals from voids.

However, theoretical calculations rely on a smooth matter-density field to define voids, while observations can only provide a discrete distribution of tracers in three dimensions. A number of different methods have recently been developed to quantitatively extract void catalogues from observations (see, e.g., Padilla et al. 2005; Neyrinck 2008; Sutter et al. 2015), but their full connection to theory remains an open problem. Given the large number of observational void catalogues already published (Pan et al. 2012; Sutter et al. 2012a; Ceccarelli et al. 2013; Mao et al. 2017; Nadathur 2016), and expected to become available with future surveys (e.g., LSST, EUCLID, DESI, see Ivezic et al. 2008; Laureijs et al. 2011; DESI Collaboration et al. 2016, respectively), it is important to address this issue. The results of Pollina et al. (2017) provide a first step to connect theory with practice, as Equation (1) allows us to bridge the gap between the matter- and tracer density profiles around observationally defined voids. In fact, these results have already been employed to this end by Ronconi & Marulli (2017), who extended their theoretical void size function to voids traced in halos thanks to Equation (1).

While the first models for void evolution (Hausman et al. 1983; Bertschinger 1985) have been developed soon after their earliest observations (Gregory et al. 1978; Kirshner et al. 1981), the previous decade has witnessed an increasing number of publications unveiling the potential of various void properties to provide new insights into cosmology. For example, their average density profile has been shown to follow a universal shape across void size, redshift, and tracer type that can be described by a narrow family of empirical functions (e.g., Ricciardelli et al. 2013, 2014; Hamaus et al. 2014c; Sutter et al. 2014a). Based on the cosmological principle, voids represent a population of statistically isotropic spheres

---

[1] Note that Nadathur & Percival (2017) find a residual from the linearity of Equation (1) when b_{slope} is fixed to the linear bias b_{t}, while Pollina et al. (2017) and this paper treats it as a free parameter.

distributed at different redshifts, allowing us to probe the expansion history of the Universe by means of the Alcock-Paczynski (AP) test (Alcock & Paczynski 1979; Lavaux & Wandelt 2012; Sutter et al. 2012b, 2014b; Hamaus et al. 2014a, 2016; Mao et al. 2017). It has been investigated whether the observed Cold Spot in the Cosmic Microwave Background (CMB) could be explained as Integrated Sachs-Wolfe (ISW) imprint caused by very large voids along the line of sight (e.g., Rees et al. 1968; Finelli et al. 2014; Kovač et al. 2014; Nadathur et al. 2014; Kovács 2018), and a final conclusion on this topic is yet to be reached; the potential of the ISW by voids is nevertheless important and still being actively investigated (e.g. Granett et al. 2008; Cai et al. 2014; Nadathur & Crittenden 2016; Kovács et al. 2017). It has further been argued that void number counts have the potential to improve on dark energy constraints (Pisani et al. 2015) and that together with their average density profile can discriminate modify gravity (Li 2011; Clampitt et al. 2013; Cai et al. 2016; Barreira et al. 2015; Zivick et al. 2015), coupled dark energy (Pollina et al. 2016), and massive neutrino (Massara et al. 2015) cosmologies from ΛCDM. These probes could also be sensitive to possible degeneracies between warm dark matter and modifications of gravity (Baldi & Villaescusa-Navarro 2016). Most recently, redshift-space distortions (RSD) around voids have been identified as a promising source of additional cosmological information (Hamaus et al. 2015, 2016; Cai et al. 2016; Chuang et al. 2017; Achitouv et al. 2017; Hawken et al. 2017; Achitouv 2017; Hamaus et al. 2017). In order to fully exploit the associated signal, a reliable model for tracer bias in void environments is indispensable, which is the subject of Pollina et al. (2017) and this work.

Despite the fact that Equation (1) has a number of interesting consequences and applications, it is challenging to test experimentally, as the dark matter density cannot be observed directly in all three dimensions. However, voids can also be used as weak gravitational (anti-)lenses to infer their projected surface mass density (Krause et al. 2013; Melchior et al. 2014; Clampitt & Jain 2015; Sánchez et al. 2017). Either a deprojection of the void lensing profiles to 3D, or a projection of tracer density profiles to 2D then allows us to constrain the bias relation in voids (Fang et al., in prep). Another possibility is to apply Equation (1) to different tracers of the matter distribution. As long as every individual tracer obeys a linear clustering bias with respect to the dark matter, the relative clustering bias between the tracers should remain linear as well. In this analysis we will make use of galaxies and galaxy clusters as two distinct tracer types. These are the most commonly available and abundant tracers in current surveys, and at the same time exhibit very different clustering properties. We will use the distribution of galaxy *clusters* to define our void sample, thanks to their higher fidelity in providing photometric redshifts and thus accurate distance estimates. The relative bias relation between galaxies and galaxy clusters will be thoroughly investigated in the vicinity of those voids. In order to provide a controlled setup, we first develop our analysis techniques based on state-of-the-art hydrodynamical simulations (MAGNETICUM). Our methods are then applied to the REDMAGIC galaxy– and REDMAPPER galaxy cluster catalogues originating from the first year of observations by the DES collaboration. Realistic mock catalogues provided by the MICE 2 project that have been constructed to specifically mimic the observations which will be used to validate our conclusions.

This paper is organized as follows: in section 2 we present all the data employed in our study (hydro-sims, DES mocks and DES data); in section 3 we describe the void finding algorithm, as well as all the methods employed to estimate the relative bias of tracers; in

Table 1. Properties of the galaxy and cluster samples in the MAGNETICUM simulations. The minimum mass M_{min} is given in terms of stellar mass M_* for galaxies, and in terms of $M_{500\mathrm{c}}$ for clusters. N_{t} is the total number of tracers and N_{v} the corresponding number of identified voids.

Tracers	$M_{\mathrm{min}}[M_\odot/h]$	N_{t}	N_{v}
Galaxies	$M_* = 1 \times 10^{11}$	6.5×10^6	-
	$M_* = 5 \times 10^{11}$	2.6×10^6	-
	$M_* = 1 \times 10^{12}$	3.5×10^5	-
Clusters	$M_{500\mathrm{c}} = 1 \times 10^{14}$	1.0×10^5	1053

section 4 we present the results of our analysis; finally we discuss our conclusions in section 5.

2 SIMULATIONS, DATA AND MOCKS

2.1 Simulations

The hydrodynamical simulation suite MAGNETICUM *pathfinder*[2] (Dolag et al, in prep.) has already been employed successfully in a wide number of numerical studies. MAGNETICUM showed so far a remarkably good agreement with observations for various probes, such as for the pressure profiles of the intra-cluster medium (Planck Collaboration et al. 2013; McDonald et al. 2014), the expected Sunyaev Zeldovich signal (Dolag et al. 2016), the imprint of the inter-galactic medium onto the dispersion signal of Fast Radio Bursts (Dolag et al. 2015), various characteristics of AGN populations (Hirschmann et al. 2014; Steinborn et al. 2015, 2016), the dynamical features of massive spheroidal galaxies (Remus et al. 2013, 2017), and the angular momentum signatures of galaxies (Teklu et al. 2015).

In this work we employ the largest cosmological volume simulated within that project, it covers a box of side length $2688h^{-1}$ Mpc, simulated using 2×4536^3 particles (for details, see Bocquet et al. 2016). We adopted a WMAP7 (Komatsu et al. 2011) ΛCDM cosmology with $\sigma_8 = 0.809$, $h = 0.704$, $\Omega_\Lambda = 0.728$, $\Omega_m = 0.272$, $\Omega_b = 0.0456$, and an initial slope for the power spectrum of $n_s = 0.963$. The simulation is based on P-GADGET3 (Springel 2005), a parallel cosmological tree Particle-Mesh (PM) Smoothed-Particle Hydrodynamics (SPH) code. It uses an entropy-conserving formulation of SPH (Springel & Hernquist 2002) and follows the gas using a low-viscosity SPH scheme to properly track turbulence (Dolag et al. 2005). Halos and sub-halos are identified using the SUBFIND algorithm (Springel et al. 2001; Dolag et al. 2009). SUBFIND identifies sub-structures as locally overdense, gravitationally bound groups of particles, starting from a main halo which is identified through the Friends-of-Friends (FoF) algorithm with a linking length of 0.16 times the mean inter-particle separation. After this first step a local density is estimated for each particle via adaptive kernel estimation, making use of a prescribed number of smoothing neighbours. After isolated density peaks are identified, additional particles of decreasing density are added. When a saddle point that connects two disjoint overdense regions in the global density field is reached, the smaller structure between the two is treated as a sub-structure candidate, and the two overdensities are then merged. An iterative unbinding procedure with a tree-based calculation of the potential is then run on all sub-structure candidates. These structures are finally associated with

---

[2] http://www.magneticum.org

galaxies, and their integrated properties (such as stellar mass, M_*) are computed. Galaxies in MAGNETICUM can have stellar masses as low as $4 \times 10^8 h^{-1} M_\odot$, but in this study we will consider as main sample only galaxies with $M_* \geqslant 10^{11} h^{-1} M_\odot$, which are more realistically observable.

The virial radius of the main haloes identified by the FoF algorithm is calculated using a density contrast built on the top-hat model (Eke et al. 1996). To allow a better comparison with observations, we additionally use an overdensity with respect to 500 times the critical density to define M_{500c}, which is the mass we will refer to as cluster mass in this paper. Clusters are identified as main haloes with $M_{500c} > 10^{13} h^{-1} M_\odot$, but in this paper we only consider MAGNETICUM clusters above $10^{14} h^{-1} M_\odot$. For our analysis we make use of the galaxy and cluster samples extracted from the simulation at redshift $z = 0.14$ with the criteria explained above. In Table 1 we summarise some properties of the tracers relevant in this work.

2.2   Data

The Dark Energy Survey (DES, see The Dark Energy Survey Collaboration 2005) is an on-going 5 year observational campaign supported by an international collaborative effort. It employs the 570 megapixel Dark Energy Camera (DECam, see Honscheid et al. 2008; Flaugher et al. 2015) mounted on the Blanco telescope at the Cerro Tololo Inter-American Observatory (CTIO). At the end of its operations, DES will have mapped approximately 300 million galaxies and tens of thousands of clusters over a 5000 square degree footprint in the southern hemisphere. DES provides photometric data using five filters (*grizY*) to the limiting magnitude of 24th *i*-band (Kessler et al. 2015), although the relevant limiting magnitude for this study is 22.5 in *i*-band, as it constrains the observations of galaxies (Drlica-Wagner et al. 2018). In this work we employ data obtained during the first year of observation (Y1) taken between Aug. 31 2013 and Feb. 9 2014, that have already shown their potential in constraining cosmology (DES Collaboration et al. 2017). DES Y1 wide-field observations scanned a large region extending approximately between $-60° < \delta < -40°$ overlapping the South Pole Telescope (SPT) survey footprint, screening an area of $1321 \deg^2$ (A1). A much smaller area overlapping the "Stripe 82" of the Sloan Digital Sky Survey (SDSS) was also mapped by DES, but this region will not be included in our analysis. From the Gold catalogues (Drlica-Wagner et al. 2018), 26 million galaxies were selected for the weak lensing sample. Recently the first three years of the observational campaign were made public with the first DES data release (Abbott et al. 2018).

2.2.1   Galaxy clusters

We make use of *red-sequence Matched-filter Probabilistic Percolation* (REDMAPPER) Y1A1 clusters (McClintock et al. 2018), both to use them as tracers of the large-scale structure, and to identify cosmic voids in the latter. The photometric red-sequence cluster finder REDMAPPER is specifically developed for large photometric surveys. It identifies galaxy clusters by searching for a bulk of its population to be made up of old, red galaxies with a prominent 4000Å-break. Focusing on this specific galaxy population the algorithm increases the contrast between cluster and background galaxies in colour space, and it enables accurate and precise photometric redshift estimates, with a scatter of $\sigma_z/(1 + z) = 0.01$ level for $z < 0.7$ (Rykoff et al. 2016), which includes the redshift window employed for data analysis in this paper. The associated cluster

richness estimator, λ, is the sum of the membership probability of every galaxy in the cluster field, and has been optimized to reduce the scatter in the richness-mass relation (Rozo et al. 2009, 2011; Rykoff et al. 2012). For a more detailed description of the algorithm we refer to Rykoff et al. (2016). In this work we will employ cluster samples with $\lambda > 5$, which corresponds to a minimum mean mass of about $\sim 10^{13} h^{-1} M_\odot$ following the mass-richness relation of McClintock et al. (2018). This low richness cut that does not guarantee the purest cluster selection. In this paper, however, we are not interested in the detailed properties of individual clusters. Rather, we desire the selected sample to be used as a tracer of large-scale structure, regardless of whether some of its objects are true clusters or not. The resulting full catalogue contains 103423 clusters and has proven to be optimal for the task of void identification, owing to its relatively high cluster density of about $10^{-4} h^3 \mathrm{Mpc}^{-3}$.

2.2.2   Galaxies

We also employ *red-sequence Matched-filter Galaxy Catalog* (REDMAGIC) Y1A1 galaxies (Elvin-Poole et al. 2017) as tracers of large-scale structure. The REDMAGIC algorithm (Rozo et al. 2016) is automated for selecting Luminous Red Galaxies (LRGs) and was specifically designed to minimize photometric redshift uncertainties in photometric large-scale structure studies, resulting in a photo-z bias $z_{spec} - z_{photo}$ better than 0.005 and in a scatter $\sigma_z/(1 + z)$ of 0.017. REDMAGIC achieves this goal by self-training the colour cuts necessary to produce a luminosity-thresholded LRG sample of constant comoving density. In this work we will distinguish among three different REDMAGIC samples, denoted as *high density* (brighter than $0.5\,L_*$ and density $10^{-3} h^3 \mathrm{Mpc}^{-3}$), *high luminosity* (brighter than $1\,L_*$ and density $4 \times 10^{-4} h^3 \mathrm{Mpc}^{-3}$), and *higher luminosity* (brighter than $1.5\,L_*$ and density $10^{-4} h^3 \mathrm{Mpc}^{-3}$).

2.3   DES Mocks

In order to validate our results, we make use of mock catalogues extracted from the MICE 2 project. MICE 2, based on the original MICE (MareNostrum - Instituto de Ciencias del Espacio) project (Crocce et al. 2015; Fosalba et al. 2015), is a suite of large high-resolution N-body simulations that have been run with the GADGET 2 code (Springel 2005). Including 4096^3 particles in a box size of $3.072 h^{-1} \mathrm{Gpc}$, MICE 2 resolves halos with even lower mass resolution ($2.93 \times 10^{10} h^{-1} M_\odot$) than MICE, making this particular simulation a perfect tool in providing mocks for deep and sensitive surveys such as DES. FoF halo catalogues extracted from the simulations are populated by galaxies using a Halo Occupation Distribution (HOD), which assigns luminosities to the central and satellite galaxies so that their observed luminosity function is preserved. The MICE 2 galaxy catalogue is forced to match luminosity, colours and clustering properties of DES at redshift $z = 0.1$, from where a light cone is then extrapolated by replicating and translating the simulation box, allowing one to build an output with negligible repetition up to redshift $z = 1.4$. In this work we are going to employ the largest available light cone, which reproduces a full octant of the sky with the same properties as the DES Y1 observations, such as photometry. More specifically, we will employ the REDMAGIC galaxy and REDMAPPER cluster catalogues extracted from MICE 2 to asses the impact of photometric redshift uncertainty on our results.

3 METHODS

3.1 Void finder

We employ the Void IDentification and Examination toolkit VIDE (Sutter et al. 2015) to construct our void catalogues. VIDE implements an enhanced version of ZOBOV (ZOnes Bordering On Voidness, Neyrinck 2008), an algorithm that identifies density depressions in a 3-dimensional set of points. The void finding procedure consists of three steps. First, the finder reads in the tracer positions and associates to each tracer a cell of volume that is closer to it than to any other tracer. This procedure is unique and referred to as *Voronoi tessellation*, the resulting cells are denoted *Voronoi cells*. By assuming equal weights for all particles it is straight-forward to associate a density to each Voronoi cell: it is simply obtained as the inverse of the Voronoi cell volume. In this manner every point inside the tracer distribution can be associated with a density, hence a well-defined density field is obtained. As a second step, local density minima are found and their surrounding basins identified. A local density minimum is a Voronoi cell of given volume whose neighbouring cells all have smaller volumes, respectively higher densities, than the central cell. Starting from these density minima, surrounding Voronoi cells are merged consecutively if their individual density is above the one of the previously merged cell. Once a cell of lower density is encountered, the process of merging is stopped. Thus, this procedure delineates local density basins, denoted as *zones*, with their surrounding ridges in the tracer distribution.

Finally, zones are merged to become voids by means of the so-called *watershed* algorithm (e.g., Platen et al. 2007). To this end a density threshold is raised starting from each zone's local density minimum. In analogy to a rising water level on a two-dimensional terrain, water flows into adjacent zones when the separating ridges are overflown. As long as shallower zones are added to the original zone, the final void consists of all such merged zones, which are still recorded as its sub-voids. When a deeper zone is encountered, the process is stopped. Therefore, the watershed algorithm naturally constructs a hierarchical structure of nested voids. Optionally, in order to prevent including very overdense structures inside voids, a density threshold for ridge densities can be set. It is typically chosen to be 20% of the mean tracer density.

In this work we will employ the most general void catalogue produced by VIDE, without applying any further selection cuts on density or hierarchy levels of voids. We define the void centre as the volume-weighted barycentre $\vec{X}$ of the N Voronoi cells that define each void,

$$\vec{X} = \sum_{i=1}^{N} \vec{x}_i \cdot V_i \Big/ \sum_{i=1}^{N} V_i , \tag{3}$$

where $\vec{x}_i$ are the coordinates of the i-th tracer of that void, and V_i the volumes of their associated Voronoi cells. The *effective* void radius r_{v} is calculated from the total volume of the void V_{v}. It is defined as the radius of a sphere with the same volume,

$$V_{\mathrm{v}} \equiv \sum_{i=1}^{N} V_i = \frac{4\pi}{3} r_{\mathrm{v}}^3 . \tag{4}$$

3.2 Correlation functions

In order to explore the clustering statistics around voids we will employ correlation functions. The two-point correlation function

$\xi_{\mathrm{t_1 t_2}}(r)$ between a tracer $\mathrm{t_1}$ and a tracer $\mathrm{t_2}$ is defined via the ensemble average

$$\xi_{\mathrm{t_1 t_2}}(r) \equiv \langle \delta_{\mathrm{t_1}}(\vec{x}) \delta_{\mathrm{t_2}}(\vec{x} + \vec{r}) \rangle , \tag{5}$$

where the spatial density fluctuation of a tracer around its average density $\langle n_{\mathrm{t}} \rangle$ is given by $\delta_{\mathrm{t}}(\vec{x}) = n_{\mathrm{t}}(\vec{x})/\langle n_{\mathrm{t}} \rangle - 1$. In the case where $\mathrm{t_1} = \mathrm{t_2}$, this statistic is referred to as *auto*-correlation function, and for $\mathrm{t_1} \neq \mathrm{t_2}$ as *cross*-correlation function. The cross-correlation function between void centres and tracers $\xi_{\mathrm{vt}}(r)$ is of particular relevance for this work. It can be shown to be equivalent to the average (or stacked) tracer-density profile of voids, $n_{\mathrm{vt}}(r)/\langle n_{\mathrm{t}} \rangle - 1$ (see Hamaus et al. 2015). In simulations that incorporate periodic boundary conditions it is straight-forward to calculate; one simply histograms the number of tracers in spherical shells of width δr around each void centre,

$$n_{\mathrm{vt}}(r) = \sum_i \frac{\Theta(|\vec{X} - \vec{x}_i| - r)}{\delta V(r)} , \tag{6}$$

and then averages it over all voids. Here Θ represents a step function with

$$\Theta(x) = \begin{cases} 1 \, , \text{for } -\delta r/2 < x < \delta r/2 \\ 0 \, , \text{otherwise} . \end{cases} \tag{7}$$

In order to suppress discreteness noise, we choose to keep the radial shell bins fixed in units of the void radius r_{v} of each void, and normalize by the constant shell volumes

$$\delta V(r) = \frac{4\pi}{3} \left[(r + \delta r/2)^3 - (r - \delta r/2)^3 \right] (\bar{r}_{\mathrm{v}}/r_{\mathrm{v}})^3 \tag{8}$$

after averaging over the tracer counts around all voids. The mean effective radius $\bar{r}_{\mathrm{v}}$ of the void sample is used to rescale from dimensionless to physical units of volume.

However, in real observations we are observing tracers inside irregular boundaries of a survey mask on the past light cone. In that situation it is helpful to employ a catalog of randoms to isolate true from fake correlations in the data. To this end the *Landy-Szalay* estimator (Landy & Szalay 1993) provides a way to calculate the void-tracer cross-correlation function from data catalogues D and random catalogues R for each tracer and void sample,

$$\xi_{\mathrm{vt}}(r) = \frac{\langle D_{\mathrm{v}} D_{\mathrm{t}} \rangle - \langle D_{\mathrm{v}} R_{\mathrm{t}} \rangle - \langle D_{\mathrm{t}} R_{\mathrm{v}} \rangle + \langle R_{\mathrm{v}} R_{\mathrm{t}} \rangle}{\langle R_{\mathrm{v}} R_{\mathrm{t}} \rangle} , \tag{9}$$

where angled brackets symbolize normalized pair counts at separation r in units of r_{v}. They can be calculated as histograms in analogy to Equation (6).

Void density profiles have been studied in detail in the recent literature (e.g., Colberg et al. 2005; Ricciardelli et al. 2013, 2014; Hamaus et al. 2014c; Sutter et al. 2014a). They typically exhibit a few very characteristic features: a deep under-dense core in the very centre, and an over-dense ridge (compensation wall) close to the effective radius r_{v}. The following empirical function was shown to capture these features accurately (Hamaus et al. 2014c),

$$\frac{n_{\mathrm{vt}}(r)}{\langle n_{\mathrm{t}} \rangle} - 1 = \delta_c \frac{1 - (r/r_s)^\alpha}{1 + (r/r_{\mathrm{v}})^\beta} , \tag{10}$$

where δ_c is the central density contrast at $r = 0$, r_s a scale radius at which the density equals the average density of tracers $\langle n_{\mathrm{t}} \rangle$, and α, β describe the inner and outer slopes of the profile.

3.3   Bias estimation

In simulations the clustering bias of any tracer can directly be calculated, because the dark matter particle locations are available. Therefore, it is simply given by the ratio of tracer and matter correlation functions,

$$b_{\mathrm{t}} = \sqrt{\frac{\xi_{\mathrm{tt}}(r)}{\xi_{\mathrm{mm}}(r)}} \simeq \frac{\xi_{\mathrm{tm}}(r)}{\xi_{\mathrm{mm}}(r)} \ . \tag{11}$$

The second equality only holds on large scales in the linear regime, where b_{t} is a constant number. In a similar manner we can define the relative bias between a tracer t_1 and a tracer t_2 as

$$b_{\mathrm{rel}} \equiv \frac{b_{\mathrm{t}_1}}{b_{\mathrm{t}_2}} = \sqrt{\frac{\xi_{\mathrm{t}_1 \mathrm{t}_1}(r)}{\xi_{\mathrm{t}_2 \mathrm{t}_2}(r)}} \simeq \frac{\xi_{\mathrm{t}_1 \mathrm{t}_2}(r)}{\xi_{\mathrm{t}_2 \mathrm{t}_2}(r)} \ , \tag{12}$$

where, without loss of generality, we may choose tracer t_1 to be the more highly biased one, such that $b_{\mathrm{rel}} > 1$. In this analysis we will associate the highly biased tracer with galaxy clusters, and the less biased tracer with galaxies.

In observational data, where we do not have direct access to the mass distribution, the absolute clustering bias of tracers can only be determined indirectly. We follow the approach of Paech et al. (2017) and calculate the angular power spectra between tracer t_1 and tracer t_2 using the public code CLASS[3] (Blas et al. 2011) and its extension CLASSgal (Di Dio et al. 2013),

$$C_{\ell}^{\mathrm{t}_1 \mathrm{t}_2} = 4\pi \int \frac{\mathrm{d}k}{k} P_{\mathrm{ini}}(k) \Delta_{\ell}^{\mathrm{t}_1}(k) \Delta_{\ell}^{\mathrm{t}_2}(k) \ . \tag{13}$$

Here, $P_{\mathrm{ini}}(k)$ is the dimensionless primordial power spectrum at wavenumber k and

$$\Delta_{\ell}^{\mathrm{t}}(k) = \int \mathrm{d}z \, b_{\mathrm{t}} \frac{\mathrm{d}N_{\mathrm{t}}(z)}{\mathrm{d}z} j_{\ell} \left[k \, r(z) \right] D(z) T(k) \ , \tag{14}$$

where $\mathrm{d}N_{\mathrm{t}}(z)/\mathrm{d}z$ is the redshift distribution and $r(z)$ the comoving distance of tracer t, j_{ℓ} the spherical Bessel function, $D(z)$ the growth factor, and $T(k)$ the transfer function. Assuming a fiducial flat ΛCDM cosmology with the parameters $h = 0.678$, $\Omega_{\mathrm{b}} = 0.048$, $\Omega_{\mathrm{m}} = 0.308$, $\sigma_8 = 0.826$, $z_{\mathrm{re}} = 11.3$ and $n_{\mathrm{s}} = 0.96$ (Planck Collaboration et al. 2014), we can then infer the effective values of b_{t_1}, b_{t_2} and their ratio (averaged within the considered redshift range) from the angular auto-power spectra of the two tracers. The angular power spectra are determined using the public code POLSPICE[4] (Szapudi et al. 2001; Chon et al. 2004) from a pixellated map of the projected tracer-density contrast on the sky. As in Paech et al. (2017), we treat the shot noise contribution to the angular power spectra as a free parameter, and consider a multipole range of $20 < \ell < 500$. The covariance of the C_{ℓ}'s is estimated via applying a jack-knife sampling of the map, splitting up the map area into 100 contiguous regions of equal size.

4   ANALYSIS

In this section we present the results of our analysis pipeline, applied to MAGNETICUM simulations, MICE 2 mocks, and finally

---

[3] http://class-code.net
[4] http://www2.iap.fr/users/hivon/software/PolSpice

DES data. We emphasize that all void catalogues employed in this paper are identified in the cluster samples at hand, regardless of the nature of the data set analysed. If needed, we refer to those voids as *cluster-voids*, to distinguish them from voids identified in a different tracer population[5].

4.1   Hydro-simulations

With the help of the fully hydro-dynamical simulations MAGNETICUM we investigate whether it is possible to use a similar approach to that presented by Pollina et al. (2017), albeit only considering clusters and galaxies as tracers. In this manner the relative bias is expected to obey similar properties as the linear bias, in analogy to Equation (1). The idea is to only use void catalogues that are defined in the most highly biased population available and then compute the average tracer-density profiles around voids of similar size using clusters and galaxies separately. The latter are hence exclusively used to compute galaxy-density profiles around cluster-voids.

We apply a conservatively high mass cut of $M_{\mathrm{min}} = 10^{14} h^{-1} M_{\odot}$ to our MAGNETICUM clusters, firstly to make sure that we do not include objects that are of too low detection significance in the observed data, and secondly to achieve a relative bias between our cluster and galaxy sample that is significantly larger than unity. Since the lower limit for the bias of the galaxy sample is set by the mass resolution of the simulation, we can only boost the relative bias by increasing M_{min} for the cluster sample. This implies a lower resolution for smaller voids due to tracer sparsity (for further details on sparse sampling and void finding, see Sutter et al. 2014a), so the resulting void catalogue contains rather large objects. However, as we are only interested in the relation between tracer-density profiles around a fixed void population, the absolute distribution of void sizes does not matter for our purposes.

In the left panel of Fig. 1 we show the stacked density profile of such cluster-voids computed twice: once using the same cluster population they were identified in (dashed black line), and once using the full galaxy sample extracted from MAGNETICUM (red dotted line). The shaded areas represent the uncertainty on the mean density profile, computed as the standard deviation of all individual void profiles from their mean. The void density profiles are calculated following the procedure explained in the beginning of Section 3.2, including voids of effective radii in the range $190 h^{-1}$Mpc $< r_{\mathrm{v}} < 220 h^{-1}$Mpc. The function from Equation (10) is used to fit the density profiles (solid black for clusters and long-dashed red for galaxies), yielding a good match in both cases. This corroborates the universal character of Equation (10) with respect to tracer type. The very characteristic features are a clear under-dense core close in the void centre and a compensation wall around $r \simeq r_{\mathrm{v}}$, which are most pronounced in the cluster-density profile. When the density profile of galaxies around the same cluster-voids is computed, those features are less pronounced, but still clearly visible. Because clusters have a higher clustering bias than galaxies, this behaviour is expected.

Our aim is to constrain the detailed relation between the two void density profiles. In particular, we want to check whether it is

---

[5] The procedure can also be inverted, i.e. it is possible define voids in the galaxy sample and then use those voids to measure the density of galaxies and clusters around them. For consistency with the approach in Pollina et al. (2017), and for the advantage that will be presented in section 4.2.1, we use the more highly biased tracer to identify voids.
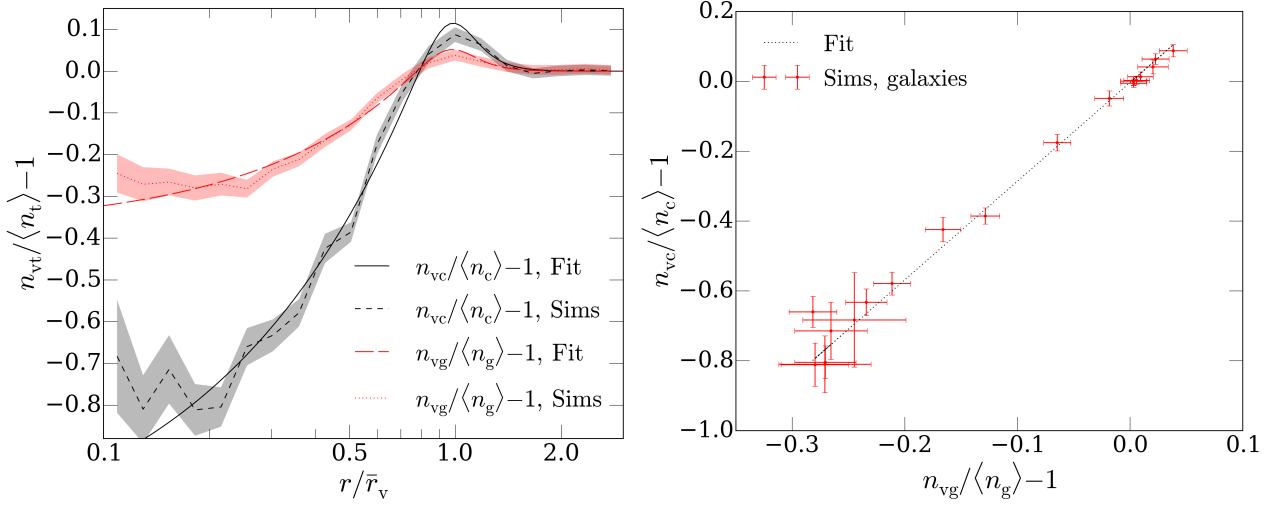
Figure 1. Left: Tracer-density profiles (dashed black for clusters, dotted red for galaxies) around cluster-defined voids of radius $190h^{-1}\mathrm{Mpc} < r_\mathrm{v} < 220h^{-1}\mathrm{Mpc}$ in the MAGNETICUM simulation. Solid black and long-dashed red lines show the best fits obtained via Equation (10). Right: Cluster- and galaxy-density profiles from the left panel plotted against each other (black points with error bars). The dotted black line shows the best fit using Equation (15).
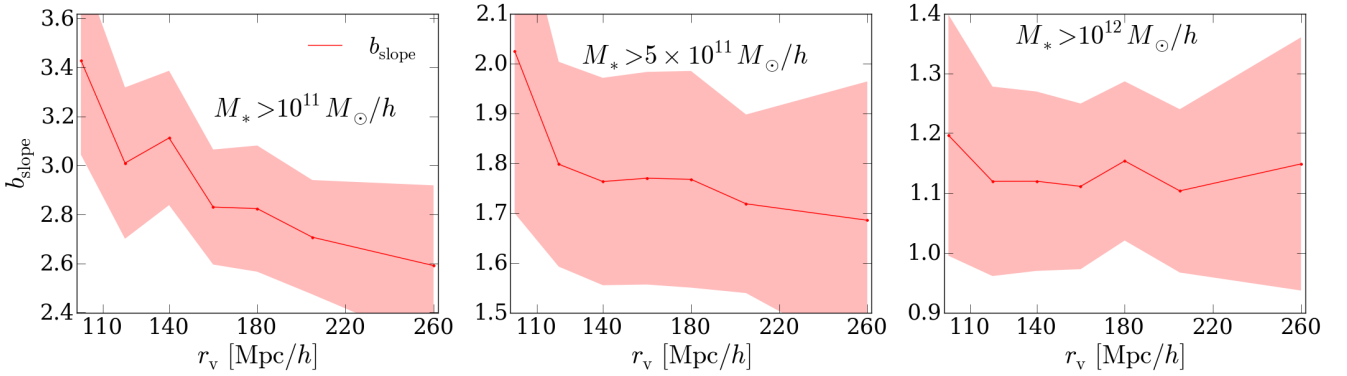

Figure 2. Best-fit values for b_slope as a function of effective void radius in the MAGNETICUM simulation. The stellar-mass cut for the galaxy sample is varied from left to right, as indicated in each panel. The cluster sample has a fixed mass cut of $M_\mathrm{500c} > 10^{14}h^{-1}M_\odot$, it is also used for the void identification.
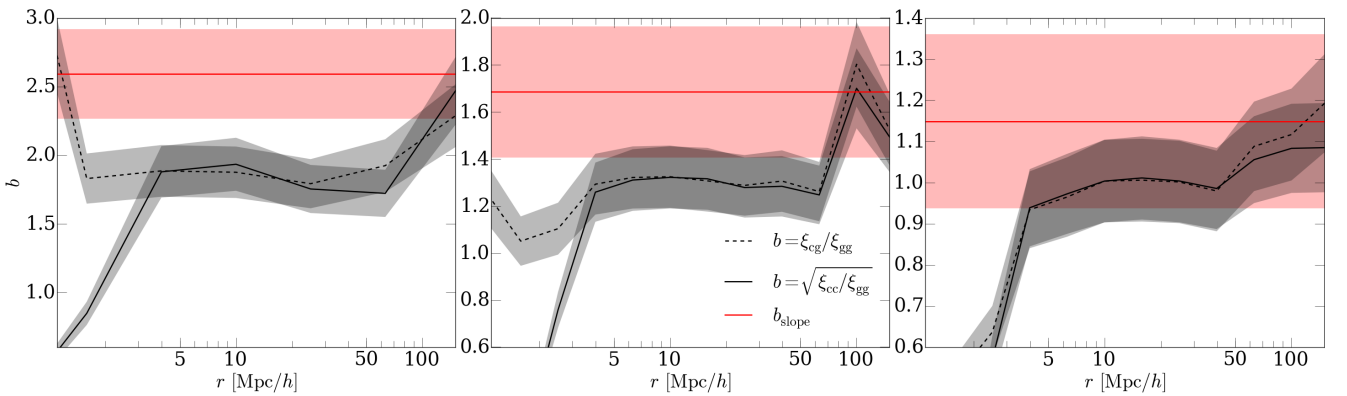
Figure 3. Comparison of the best-fit b_slope obtained from our largest void sample (solid red line) to the relative bias b_rel between clusters and galaxies in the MAGNETICUM simulation, calculated using the estimators as indicated (black dashed and dotted lines). The stellar-mass cut for the galaxy sample is varied from left to right, with the same values as in Fig. 2.

Table 2. Best-fit values and 1σ uncertainties on the parameters of Equation (15) for cluster-defined voids of various size and for different stellar-mass cuts in the galaxy sample from the MAGNETICUM simulation.

Voids	Galaxies ($M_* > 1 \times 10^{11} h^{-1} M_\odot$)		Galaxies ($M_* > 5 \times 10^{11} h^{-1} M_\odot$)		Galaxies ($M_* > 1 \times 10^{12} h^{-1} M_\odot$)	
Bins in $r_{\rm v}$ [h^{-1}Mpc]	$b_{\rm slope}$	$c_{\rm offset}$	$b_{\rm slope}$	$c_{\rm offset}$	$b_{\rm slope}$	$c_{\rm offset}$
$90 < r_{\rm v} < 110$	3.43 ± 0.39	-0.033 ± 0.089	2.02 ± 0.33	-0.013 ± 0.095	1.20 ± 0.21	-0.005 ± 0.022
$110 < r_{\rm v} < 130$	3.01 ± 0.10	-0.009 ± 0.070	1.80 ± 0.21	-0.003 ± 0.064	1.12 ± 0.14	-0.001 ± 0.020
$130 < r_{\rm v} < 150$	3.11 ± 0.26	-0.009 ± 0.063	1.76 ± 0.20	-0.005 ± 0.063	1.12 ± 0.14	-0.000 ± 0.055
$150 < r_{\rm v} < 170$	2.83 ± 0.22	-0.007 ± 0.045	1.77 ± 0.22	-0.003 ± 0.063	1.11 ± 0.14	-0.001 ± 0.045
$170 < r_{\rm v} < 190$	2.82 ± 0.26	-0.003 ± 0.063	1.77 ± 0.20	-0.001 ± 0.061	1.15 ± 0.14	-0.002 ± 0.045
$190 < r_{\rm v} < 220$	2.71 ± 0.22	-0.009 ± 0.045	1.72 ± 0.17	-0.004 ± 0.060	1.10 ± 0.14	-0.002 ± 0.055
$220 < r_{\rm v} < 250$	2.59 ± 0.33	-0.035 ± 0.105	1.68 ± 0.28	-0.017 ± 0.101	1.15 ± 0.22	-0.000 ± 0.095

linear, similar to the relation between tracers and mass found in Pollina et al. (2017). To this end we plot the cluster-density profile $\xi_{\rm vc}(r)$ as a function of the corresponding galaxy-density profile $\xi_{\rm vg}(r)$ of the same cluster-voids. The results are depicted as red dots in the right panel of Fig. 1, where the error bars show the uncertainty on the mean density profiles from the left panel. The following simple linear function is used to fit those data points (black dotted line):

$$\xi_{\rm vc}(r) = b_{\rm slope}\xi_{\rm vg}(r) + c_{\rm offset} \;, \qquad (15)$$

where $b_{\rm slope}$ and $c_{\rm offset}$ are the only two free parameters of the fit. The linear relation between $\xi_{\rm vc}(r)$ and $\xi_{\rm vg}(r)$ is evident, and in concordance with the linearity between $\xi_{\rm vc}(r)$ and the matter-density profile $\xi_{\rm vm}(r)$ from earlier work (Pollina et al. 2017). The best-fit values for $b_{\rm slope}$ and $c_{\rm offset}$, including their 1σ uncertainties can be found in Table 2. $c_{\rm offset}$ is compatible with zero within the error, while $b_{\rm slope}$ attains a value of about 2.7. We expect $b_{\rm slope}$ to be related to the relative bias between clusters and galaxies, in analogy to Equation (12).

We repeated the previous analysis for voids of different size, and confirmed the linear relation in Equation (15) to provide a good fit in all cases. The best-fit values of $b_{\rm slope}$ and $c_{\rm offset}$ are summarized in Table 2. Furthermore, we explored the impact of various mass cuts in our galaxy sample. The overall clustering amplitude of galaxies is expected to depend on their stellar mass, which should be reflected in our best fit for $b_{\rm slope}$ as well. While our original sample contained all galaxies with stellar mass above $1 \times 10^{11} h^{-1} M_\odot$, we impose two more restrictive cuts with $M_* > 5 \times 10^{11} h^{-1} M_\odot$ and $M_* > 1 \times 10^{12} h^{-1} M_\odot$. Also for these cases we can confirm the linear relation of Equation (15) to perform a good fit. The corresponding parameter constraints are reported in Table 2.

In Fig. 2 the best-fit values of $b_{\rm slope}$ are shown as a function of the mean effective radius of the selected void sample. The three panels correspond to the different stellar-mass cuts applied to the galaxy catalogue. We observe a clear trend of $b_{\rm slope}$ decreasing with void size, a similar behaviour of what has been presented in Pollina et al. (2017), albeit the different setup. In that study $b_{\rm slope}$ converges to a constant value for voids larger than a critical size, and this value is shown to coincide with the linear bias of the tracer with respect to the matter distribution.

In this paper, however, we are comparing the density profiles of two different tracers against each other, consequently we expect $b_{\rm slope}$ to converge towards the ratio of the linear bias parameters of both tracers, the linear relative bias $b_{\rm rel}$. We can estimate $b_{\rm rel}$ via Equation (12) in two ways, both of which are plotted in Fig. 3 as solid and dashed black lines with shaded error bars, respectively.

On large scales both estimators agree with each other, and yield the linear relative bias between the two tracers. We compare this value with the best fit for $b_{\rm slope}$ obtained from the largest effective radius bin of our void sample (red solid line with shaded error bar), which is the most likely one to have converged towards $b_{\rm rel}$. In the different panels of Fig. 3 only the stellar-mass cut for the galaxy sample is varied, with the same values as used in Fig. 2.

As evident from Fig. 3, the convergence of $b_{\rm slope}$ towards $b_{\rm rel}$ is not complete in all cases. Only for the highest stellar-mass cut of $M_* > 10^{12} h^{-1} M_\odot$ in the galaxy sample are the two values consistent with each other within the errors. At the same time, the relative bias attains the lowest value in this case, owing to the higher bias of the galaxy sample. The lower the stellar-mass cut for the galaxies, the lower becomes their bias. Therefore the relative bias between clusters and galaxies increases, which also increases the discrepancy between $b_{\rm slope}$ and $b_{\rm rel}$. Hence, the higher the relative bias between two tracers, the larger becomes the critical void radius $r_{\rm v}^+$ at which $b_{\rm slope}$ and $b_{\rm rel}$ converge. When voids are defined in sparse tracer distributions, such as the galaxy clusters considered here, the size of $r_{\rm v}^+$ may fall well beyond the range of effective void radii that can be found in the entire void sample. A similar conclusion has already been drawn in Pollina et al. (2017), where the value of $r_{\rm v}^+$ was investigated for voids identified in denser tracer samples.

Nevertheless, this first test shows that the findings of Pollina et al. (2017) can be indeed reproduced by measuring the relative bias with the analysis proposed in this section, which can be fully implemented with observational data.

4.2 DES Mocks

Having confirmed a linear relationship between the densities of luminous tracers in void environments using the MAGNETICUM simulation, we now want to move to more realistic data. The next step is to test our pipeline on DES mocks (MICE 2, see Section 2.3), to evaluate the impact of the light cone and photometric redshift uncertainty. The latter has so far been considered as an insurmountable obstacle for the identification of three-dimensional voids, as the typical photo-z scatter of a single galaxy corresponds to line-of-sight distance errors that are comparable to the extent of most voids. This limitation lead to other innovative ideas on how to investigate the potential of voids for cosmology, which explored under-dense regions of large-scale structure in two-dimensional projections on the sky (Sánchez et al. 2017; Gruen et al. 2016). It has been demonstrated how this approach opens up complementary ways to constrain cosmology (Barreira et al. 2015; Gruen et al. 2017; Friedrich et al. 2017; Cautun et al. 2017). Nevertheless, as the properties of
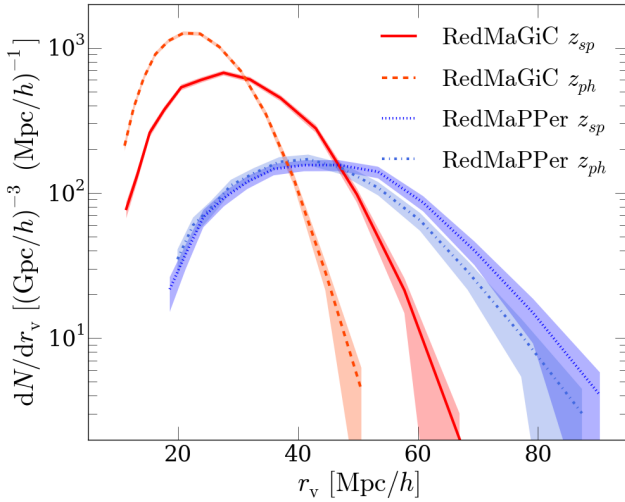
Figure 4. The abundance of voids identified in the galaxy and cluster samples of the MICE 2 mocks, as a function of their effective radius. Both photometric and spectroscopic redshifts have been used in each case, as indicated in the figure legend. The cluster-void size function is not significantly affected by photo-z uncertainty. In fact, clusters provide the most accurate photometric redshift measurements and cluster-voids are the largest voids, further reducing the relative impact of photo-z scatter on void finding.

three-dimensional voids have already been extensively studied in simulations and spectroscopic surveys (see references in the introduction), it is worth testing a similar method with photometric data.

4.2.1 *Redshift uncertainty and void finding*

To evaluate the impact of photometric redshift uncertainty on void finding we run VIDE on the REDMAGIC and REDMAPPER samples of the MICE 2 mocks twice: once using the spectroscopic redshift (spec-z), and once the photometric (photo-z) redshift estimate of each object. The photo-z scatter inherent in the latter effects the distance estimation and causes the distribution of objects to be smeared out along the line of sight.

In Fig. 4 we present the void size function (i.e., the spatial number density of voids as a function of their effective radius) in the MICE 2 mocks, extracted using VIDE on both spectroscopic and photometric samples of galaxies and clusters. While the abundance of galaxy-voids (solid and dashed red) is heavily skewed by photo-z scatter, cluster-voids (dotted and dash-dotted blue) remain surprisingly unaffected by the choice of redshift estimate. In particular, the number of galaxy-voids with $\bar{r}_v < 35h^{-1}$ Mpc is clearly overestimated when using photo-z, while the opposite is the case for larger galaxy-voids. This finding is different to what has previously been seen in Sánchez et al. (2017), where the largest galaxy-voids in the REDMAGIC sample were least affected by photo-z uncertainty. The disagreement is most likely a consequence of the different void finding techniques. The fact that Sánchez et al. (2017) utilized a two-dimensional void finder on projected slices, with a line-of-sight width above the typical photo-z scatter, largely mitigates the effects of the latter. In contrast, VIDE directly operates on three-dimensional particle distributions, and the photo-z scatter results in an unphysical line-of-sight smearing of structures that can be detected as spurious watershed ridges in the algorithm. The result is that larger voids are more likely to be segmented into multiple smaller voids.

However, this effect on void abundance is hardly detected in the cluster-void sample, thanks to the relatively accurate photometric redshift estimates in REDMAPPER clusters. The higher accuracy can be attributed to the fact that multiple member galaxies can contribute to a single cluster redshift estimate. Moreover, the sparser and more biased distribution of clusters results in larger voids overall (Sutter et al. 2014a), so the extent of the photo-z scatter in redshift space matters less in comparison to the void size. In order to quantify the impact of photometric redshifts on void identification in more detail, a comparison on individual voids would be needed. However, this goes beyond the scope of this paper, as we are only concerned about summary statistics here.

The robustness of the void size function from cluster-voids in the presence of photo-z scatter has promising consequences for void science with photometric surveys. For example, void number counts can be used to constrain cosmology (Pisani et al. 2015), even when identified in various tracer distributions. In particular, Ronconi & Marulli (2017) suggest a simple way to extend the prediction of void abundances to potentially observable voids: making use of Equation (1) they claim to be able to accurately forecast the void size function obtained from halos based on results from the excursion-set theory for dark matter voids. According to Fig. 4, this method may straight-forwardly be extended to cluster-voids extracted from photometric samples, opening up to the possible exploitation of the void size function as a cosmological probe in a large variety of forthcoming surveys (e.g., LSST, EUCLID, DESI, see Ivezic et al. 2008; Laureijs et al. 2011; DESI Collaboration et al. 2016)

4.2.2 *Density profiles and tracer bias*

We now repeat the analysis of Section 4.1 with the MICE 2 mocks, using photometric redshifts for both REDMAGIC and REDMAPPER samples. The density profiles are estimated with the help of random catalogues, to account for the mask and light-cone effects. To this end, we approximate the Landy-Szalay estimator of Equation (9) as

$$\xi_{vt}(r) \simeq \langle D_v D_t \rangle - \langle D_v R_t \rangle \,, \tag{16}$$

which was shown to yield accurate results on void scales (Hamaus et al. 2017). We have also compared our measurements with the more common Davis-Peebles estimator (Davis & Peebles 1983), which features a ratio instead of a subtraction in Equation (16), and found consistent results. Fig. 5 presents the corresponding tracer-density profiles for REDMAPPER-defined voids of size $50h^{-1}$Mpc $< r_v < 60h^{-1}$Mpc. Overall we obtain smaller void sizes from this sample, as the number density of clusters here exceeds the one analysed in MAGNETICUM. However, as MICE 2 resolves galaxies of lower mass, this results in a similar relative bias between the tracers considered. As tracers, we utilize REDMAPPER clusters of richness $\lambda > 5$, and three REDMAGIC samples with varying luminosity cuts. The correspondence with our earlier simulation results in the left panel of Fig. 1 is striking: we observe a more pronounced cluster-density profile with a deeper core and a higher ridge (dashed black line) than each of the galaxy-density profiles (dotted red line). Yet, the shapes of all these profiles seem to match quite nicely, which means that galaxies trace voids just as the clusters do, albeit with a lower clustering amplitude. This is further confirmed by the successful interpolation of all profiles by means of the fitting function presented in Equation (10) (solid black and long-dashed red lines). Note that in some cases the normalization of the profiles
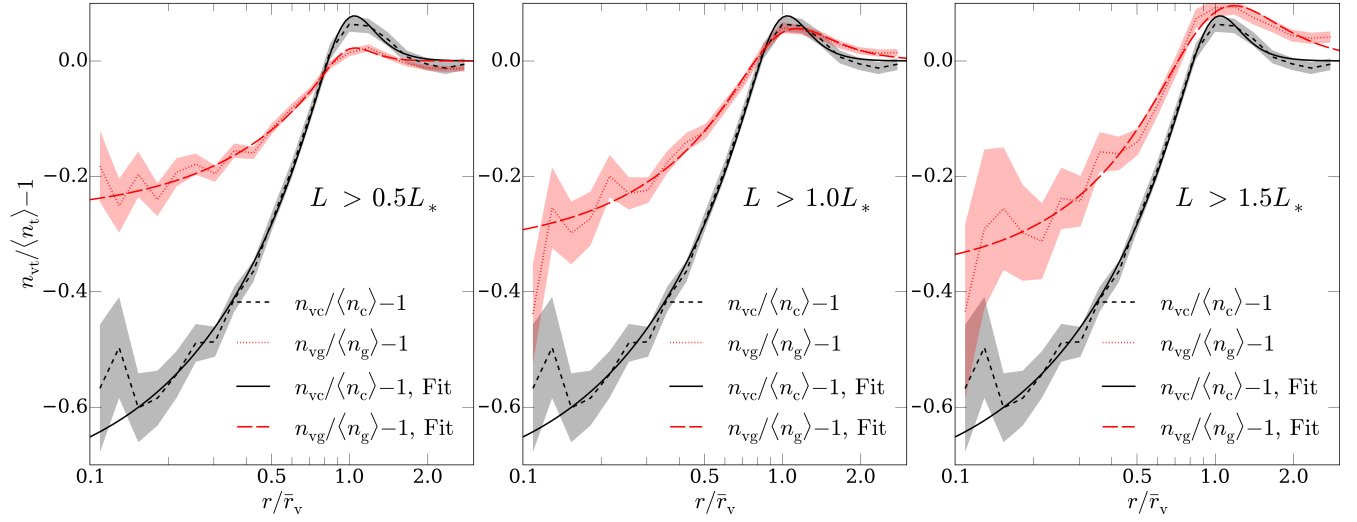
Figure 5. Tracer-density profiles (solid black for REDMAPPER clusters, dashed red for REDMAGIC galaxies) around cluster-defined voids of size $50h^{-1}$Mpc $< r_v < 60h^{-1}$Mpc in the MICE 2 mocks. The luminosity cut for the galaxy sample is varied from left to right, as indicated in each panel.
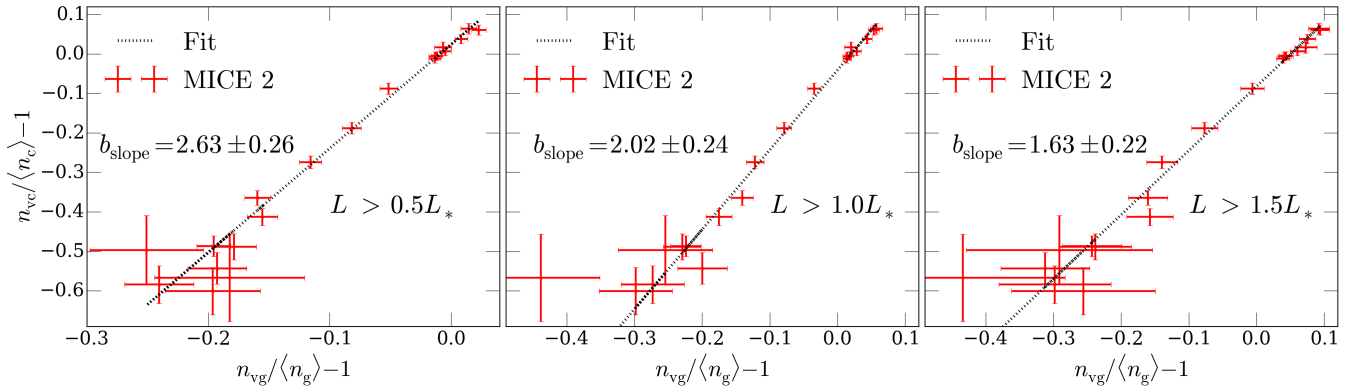

Figure 6. Cluster- and galaxy-density profiles from Fig.5 plotted against each other. The dotted black line shows the best fit obtained with Equation (15).
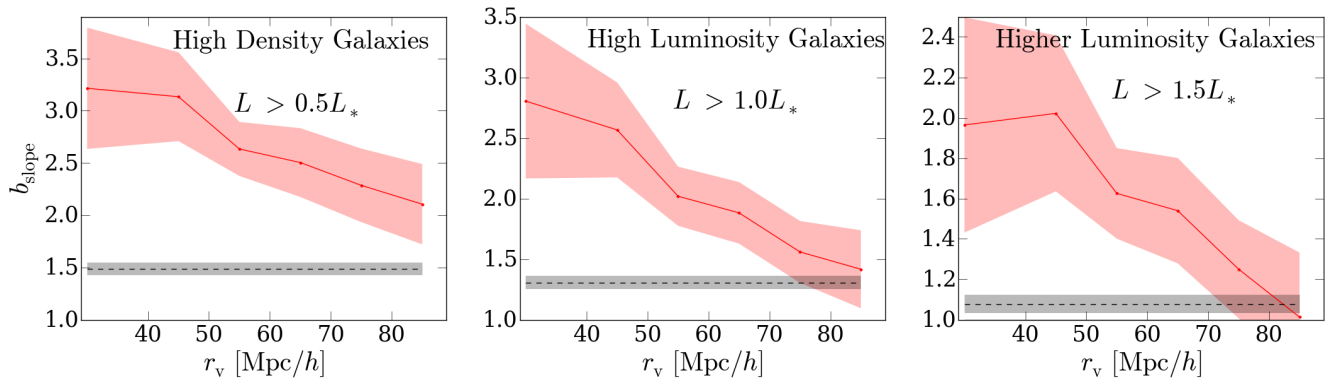

Figure 7. Best-fit values for b_{slope} (solid red) as a function of effective void radius in the MICE 2 mocks. The luminosity cut for the galaxy sample is varied from left to right, as indicated in each panel. Dashed black lines show the linear relative bias between clusters and galaxies, estimated via their angular power spectra on large scales.

Table 3. Best-fit values and 1σ uncertainties on the parameters of Equation (15) for cluster-defined voids of various size and for different luminosity cuts in the galaxy sample from the MICE 2 mocks.

Voids	REDMAGIC ($L > 0.5L_*$)		REDMAGIC ($L > 1.0L_*$)		REDMAGIC ($L > 1.5L_*$)	
Bins in r_v [h^{-1}Mpc]	b_slope	c_offset	b_slope	c_offset	b_slope	c_offset
$20 < r_\mathrm{v} < 40$	3.21 ± 0.57	-0.071 ± 0.130	2.80 ± 0.64	-0.119 ± 0.173	1.96 ± 0.53	-0.084 ± 0.158
$40 < r_\mathrm{v} < 50$	3.13 ± 0.42	-0.006 ± 0.084	2.56 ± 0.39	-0.066 ± 0.089	2.02 ± 0.39	-0.090 ± 0.10
$50 < r_\mathrm{v} < 60$	2.63 ± 0.27	0.023 ± 0.063	2.02 ± 0.23	-0.041 ± 0.063	1.62 ± 0.22	-0.082 ± 0.091
$60 < r_\mathrm{v} < 70$	2.50 ± 0.33	0.070 ± 0.105	1.88 ± 0.24	-0.043 ± 0.077	1.54 ± 0.26	-0.111 ± 0.183
$70 < r_\mathrm{v} < 80$	2.28 ± 0.35	0.101 ± 0.126	1.56 ± 0.25	-0.067 ± 0.084	1.25 ± 0.24	-0.174 ± 0.190
$80 < r_\mathrm{v} < 90$	2.10 ± 0.39	0.162 ± 0.161	1.41 ± 0.32	-0.127 ± 0.128	1.01 ± 0.31	-0.262 ± 0.354

at large distances r can be slightly offset from zero. This can have various reasons, which may be related to imperfect corrections for the survey geometry, or the spread in void sizes in a given bin of r_v. However, we have checked that the magnitude of this effect is small enough not to impact our conclusions (i.e., c_offset is always consistent with zero).

The correspondence between the different tracers can be seen more clearly in Fig. 6, where their void-centric density profiles are plotted against each other. A linear trend in the data is apparent, so we fit Equation (15) and constrain its slope and offset again. We further repeat this for voids of all available sizes from our catalogue and summarize the results in Table 3. The best-fit value for b_slope decreases when galaxies with higher luminosity cut are used. This is consistent with expectation, as they acquire a higher clustering bias, making the relative bias between clusters and galaxies decrease. In contrast, the parameter c_offset remains consistent with zero in all cases.

The dependence of b_slope on void effective radius is visualized in Fig. 7. We observe a decreasing trend again, as before in the MAGNETICUM simulation. Towards the largest voids, b_slope converges to the linear relative bias between the cluster and the galaxy samples (dashed black line), which is estimated via the method described in Section 3.3. However, the critical void radius r_v^+, where the two relative bias measurements agree, cannot be determined from the galaxy sample with the lowest luminosity cut. This confirms our earlier conclusion that the convergence of b_slope to b_rel happens at larger void radii when b_rel is higher. However, we have a clear indication that it is possible to measure the relative linear bias of tracers with this method when applied to the final DES dataset after 5 years of observations. We further conclude that the uncertainty inherent in photometric redshift estimates is not affecting our results from before: the linear relation of Equation (1) is still satisfied to the same degree of accuracy as in simulations, with similar constraints on its parameters.

4.3 Data

Having assessed the feasibility of our analysis using mocks, we are finally ready to test it on DES Y1 data and to determine whether the linear relation given by Equation (1) (applied to visible tracers) is in the sky. In this section we describe the void catalogue obtained from the data and present all related results.

4.3.1 DES void catalogue

This section presents the first catalogue of three-dimensional watershed voids built with DES data. We follow our previous approach,
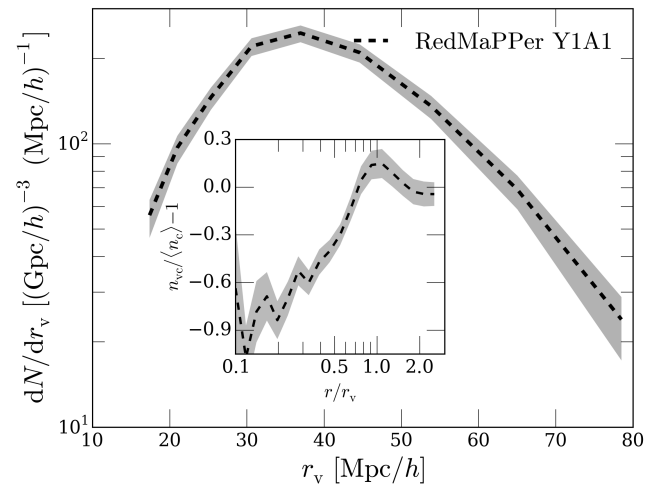
Figure 8. Abundance of voids as a function of their effective radius, identified in the distribution of REDMAPPER clusters from DES data (Y1A1). The average cluster-density profile of all voids is shown as inset.

using REDMAPPER clusters with $\lambda > 5$ for void identification with VIDE. Since the area observed during the first year of DES (Y1A1) operations is significantly smaller ($1321\deg^2$) than the full octant of the MICE 2 mocks, the number statistics of the data are expected to be lower. In total we find 475 voids in the redshift range $0.2 < z < 0.65$ (which is the range where all REDMAGIC samples are fairly volume limited), with effective radii between $15h^{-1}$Mpc and $80h^{-1}$Mpc. Voids intersecting with the survey mask have been pruned from the final sample. The void size function is shown in Fig. 8, with an inset displaying the average cluster-density profile of all voids in the sample. It is remarkably similar to that of cluster-voids in mocks shown in Fig. 4. The small difference can be caused by the assumed mass-richness relation in the cluster mocks, which may not reproduce the real data exactly.

The footprint of our void catalogue on the sky can be perceived in Fig. 9, which was made using the public code SKYMAP-PER[6]. We show the positions of void centres (cyan circles) on the density plot of clusters for a redshift slice of $0.2 < z < 0.45$. This range was chosen to allow direct comparison with Fig. 1 of Gruen et al. (2017), where a similar map for the location of line-of-sight under-densities in the galaxy spatial distribution was presented. The blue line displays the full DES footprint at the end of its operations.
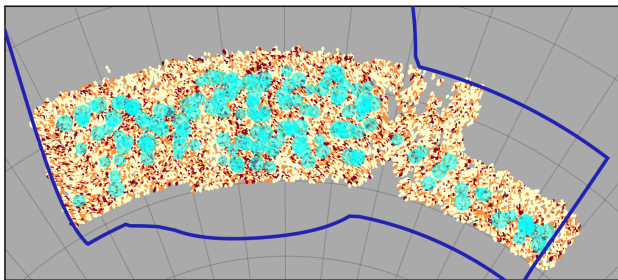
---

[6] https://github.com/pmelchior/skymapper

Figure 9. Density plot of REDMAPPER clusters and their associated void centres (cyan circles) in a redshift slice of $0.2 < z < 0.45$. The blue line displays the 5-year-DES footprint, voids intersecting with the survey mask are discarded.
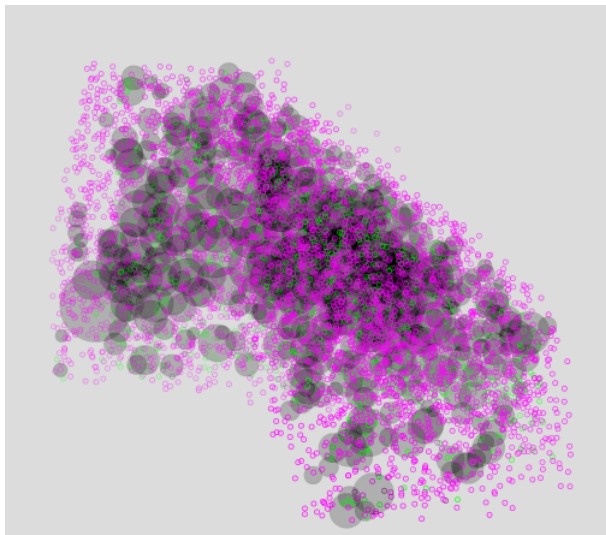

Figure 10. Three-dimensional map of the DES light cone; magenta dots show 5% of all REDMAPPER clusters, green dots display 5% of REDMAPPER clusters inside watershed voids and black spheres of radius $r_{\rm v}$ represent the spherical volume of each void.

Figure 10 is a three-dimensional plot of the DES light cone, where 5% of all REDMAPPER clusters are shown in magenta, 5% of those clusters located inside voids are highlighted in green, and black spheres of radius $r_{\rm v}$ indicate the locations of void centres with a size that reflects the spherical equivalent of the watershed volume. The number of clusters was diluted for visualization purposes.

4.3.2 Density profiles and tracer bias

With the observational void catalogue at hand, we are now in the position to apply our earlier analysis to real data. Fig. 11 features the average tracer density profiles for cluster-voids of size $40h^{-1}{\rm Mpc} < r_{\rm v} < 80h^{-1}{\rm Mpc}$. As tracers, we use REDMAPPER clusters (dashed black lines) and REDMAGIC galaxies of high density, high luminosity, and higher luminosity samples (dashed red lines, from left to right). As apparent from each panel, the densities of different tracers are highly correlated in these void environments, all featuring a clear depression around the void centre, and a compensating ridge at the void edge. In particular, the similarity with the mocks in Fig. 5 is striking, as is the ability of Equation (10) to

accurately fit the data (solid black and long-dashed red lines). However, due to the smaller area it can be noted that the uncertainties in the real data are higher, especially close to the void centres, where the statistics are most affected by the sparsity of tracers.

This can also be observed in Fig. 12, where we focus on the relation between cluster- and galaxy-density profiles plotted against each other. The linear trend in the data is apparent, although some of the data points exhibit large scatter. In all cases we find Equation (15) to provide a satisfactory fit to the data. We find no evidence for any deviation from linearity other than due to statistical noise, which argues Equation (15) to indeed be the simplest and most conservative model that is consistent with the data. Our earlier results based on simulations and mocks with much better statistics corroborate this result. We further confirm a decrease in the best-fit value of the slope $b_{\rm slope}$, caused by an increase in the bias of the galaxy samples with increasing luminosity cuts. At the same time, the offsets $c_{\rm offset}$ remain consistent with zero. The detailed parameter constraints are reported in Table 4.

Finally, we test the convergence of $b_{\rm slope}$ to the linear relative bias $b_{\rm rel}$ of the employed tracers. Due to the relatively low number of voids in our sample, we can only afford to have two independent bins in effective radius. We choose to split the sample such that both bins roughly contain the same number of voids, with $r_{\rm v} < 40h^{-1}{\rm Mpc}$ and $r_{\rm v} > 40h^{-1}{\rm Mpc}$. The corresponding best-fit values of $b_{\rm slope}$ are shown as the red dots, connected by a solid line in Fig. 13 (which is analogous to Fig. 7 albeit with DES data). In comparison, the linear relative bias estimated via the large-scale clustering statistics of the tracers, as described in Section 3.3, is shown in dashed black. Evidently, the poor statistics in the measurement do not allow any detailed conclusions about the convergence properties of $b_{\rm slope}$ towards $b_{\rm rel}$. However, at least for the galaxy samples of high and higher luminosity, an indication for a decrease in $b_{\rm slope}$ at larger $r_{\rm v}$ is apparent. A more detailed investigation of this will be possible with future DES tracer catalogues of larger size. The final DES Y5 tracer catalogues will provide similar statistics as the MICE 2 mocks employed above.

5   CONCLUSIONS

The aim of this paper was to probe the nature of tracer bias in void environments, a regime of large-scale structure that so far has little been investigated specifically for this purpose (however, see Neyrinck et al. 2014; Yang et al. 2017; Paranjape et al. 2017). In contrast, the overall tracer bias, which is typically weighted towards the most overdense structures in the Universe, has remained an active topic of research for a long time, due to its complex non-linear behaviour on intermediate and small scales (e.g., Smith et al. 2007; Cacciato et al. 2012; Springel et al. 2018; Simon & Hilbert 2017; Dvornik et al. 2018, and references therein). Moreover, recent evidence for additional stochasticity beyond the Poisson expectation in the clustering properties of galaxies and clusters further complicates the common treatment of bias (e.g. Hamaus et al. 2010; Baldauf et al. 2013; Paech et al. 2017; Gruen et al. 2017; Friedrich et al. 2017). A consistent and reliable framework for the modelling of tracer bias is indispensable for the cosmological analysis of modern data sets of large-scale structure, because it establishes a connection between its observable luminous constituents and the invisible dark matter. As the latter is expected to be responsible for more than 80% of the mass content in the Universe, the accuracy of cosmological constraints is often limited by the degree to which tracer bias is understood.
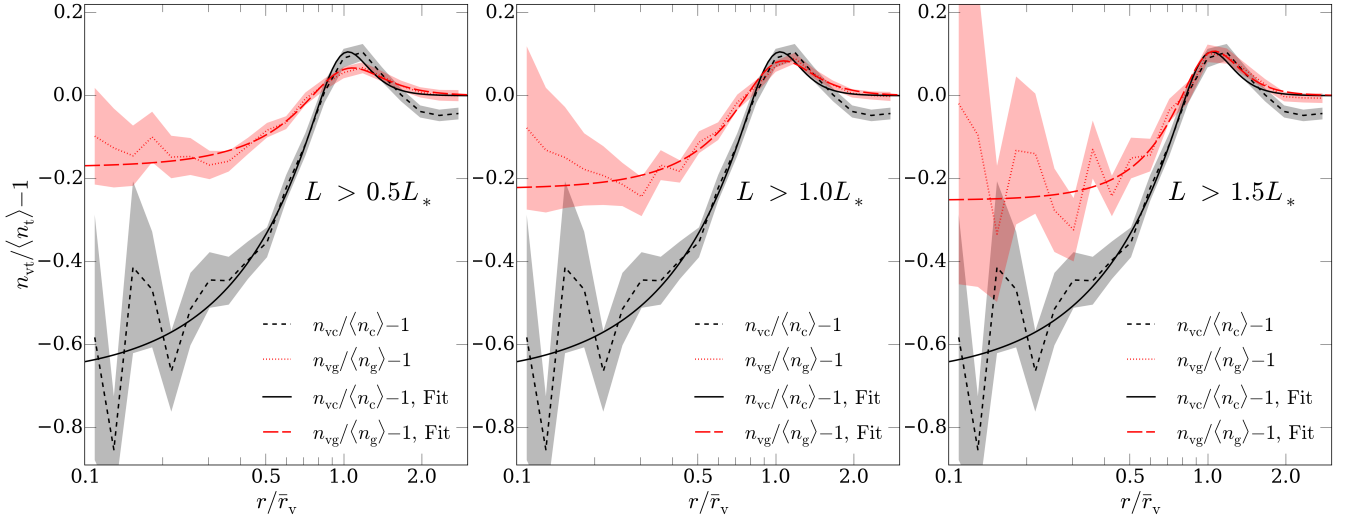
Figure 11. Tracer-density profiles (solid black for REDMAPPER clusters, dashed red for REDMAGIC galaxies) around cluster-defined voids of size $40h^{-1}$Mpc $< r_{\mathrm{v}} < 80h^{-1}$Mpc in the DES data. The luminosity cut for the galaxy sample is varied from left to right, as indicated in each panel.
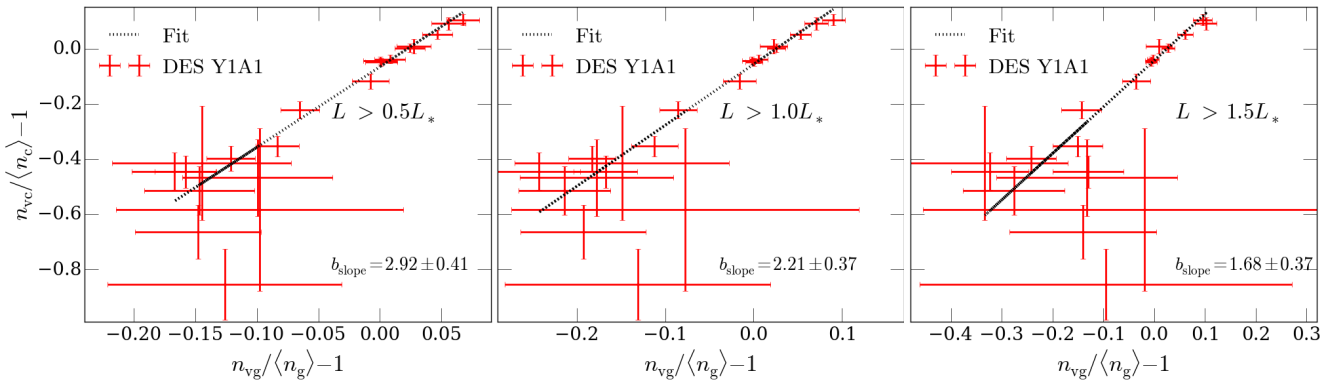

Figure 12. Cluster- and galaxy-density profiles from Fig.11 plotted against each other. The dotted black line shows the best fit obtained with Equation (15).
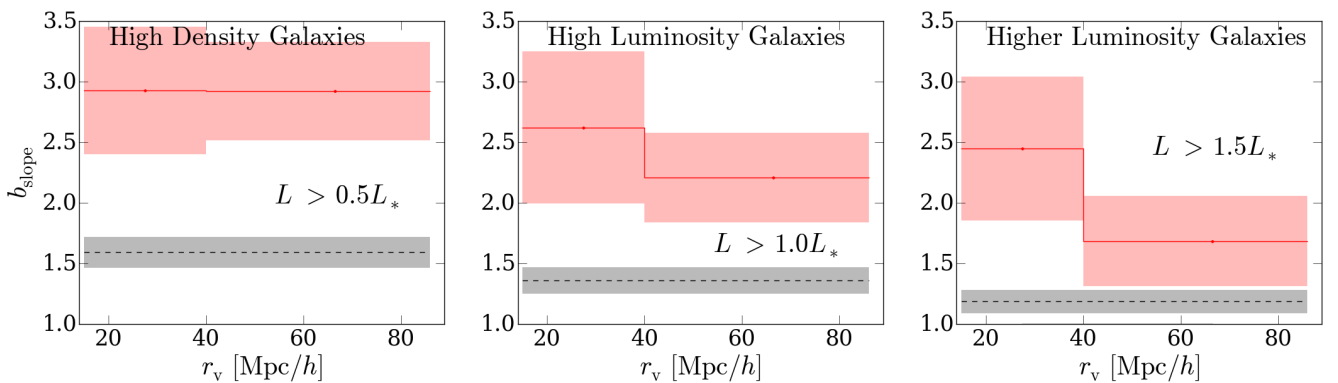

Figure 13. Best-fit values for b_{slope} (solid red) as a function of void radius in DES data. The luminosity cut for the galaxy sample varies from left to right, as indicated in each panel. Dashed black lines show the linear relative bias between clusters and galaxies, estimated via their angular power spectra on large scales.

In this work we have investigated tracer bias in void environments of the distribution of galaxy clusters, based on a complete pipeline of hydrodynamical simulations, mocks, and data from the first year of DES observations. We find a remarkably linear relationship between the void-centric density fluctuations of clusters

and galaxy samples of various magnitude limits across all distance scales, suggesting tracer bias to remain linear in the two-point statistics of void environments. This confirms recent simulation results by Pollina et al. (2017), but for the first time with observational data. We show that the relative clustering amplitude

Table 4. Best-fit values and 1σ uncertainties on the parameters of Equation (15) for cluster-defined voids of various size and for different luminosity cuts in the galaxy sample from the DES data.

Voids	REDMAGIC ($L > 0.5L_*$)		REDMAGIC ($L > 1.0L_*$)		REDMAGIC ($L > 1.5L_*$)	
Bins in r_v [h^{-1}Mpc]	b_slope	c_offset	b_slope	c_offset	b_slope	c_offset
$15 < r_\mathrm{v} < 40$	2.92 ± 0.53	-0.055 ± 0.122	2.62 ± 0.62	-0.038 ± 0.145	2.45 ± 0.59	-0.027 ± 0.138
$40 < r_\mathrm{v} < 86$	2.91 ± 0.40	-0.065 ± 0.083	2.21 ± 0.37	-0.056 ± 0.084	1.68 ± 0.37	-0.043 ± 0.095

between any two tracers can be expressed by a single multiplicative constant b_slope, relating their void-tracer cross-correlation functions according to Equation (15) with an offset consistent with zero ($c_\mathrm{offset} = 0$). However, the constant b_slope coincides with the linear relative bias b_rel between those tracers only when voids above a certain critical effective radius r_v^+ are used in this measurement. In case of very sparse void tracers, such as the galaxy clusters used here, the value of r_v^+ may exceed the available range of void sizes in a given area on the sky. For smaller voids, b_slope increases towards lower r_v.

A detailed model for this behaviour can be important in cases where the absolute value of tracer bias is needed to obtain parameter constraints, which goes beyond the scope of this paper. It has been pointed out that tracer environment can be more relevant than host-halo mass to determine the bias of tracers (Abbas & Sheth 2007; Pujol et al. 2017; Shi & Sheth 2018), and we expect the environmental constraint from voids to be important in this respect. When tracers are selected above some mass or luminosity threshold, as done here, they are typically more biased in void environments than elsewhere in the cosmic web (Yang et al. 2017; Paranjape et al. 2017). Conversely, selecting the most extreme environments as tracers of the density field, such as the centres of voids, can lead to a vanishing, or even negative clustering bias (Hamaus et al. 2014b; Clampitt et al. 2016). Nevertheless, the fact that tracer bias can be treated linearly with a single free parameter significantly simplifies most common two-point clustering analyses of large-scale structure. For example, it implies that different tracer-density profiles around voids can be described with the same universal functional form (as provided by Equation (10), Hamaus et al. 2014c; Sutter et al. 2014a). The analysis we presented is arguably the best approach to test such a function, as with observational data we do not have access to the entire three-dimensional distribution of luminous and dark matter. Furthermore, the presented method can be augmented with measurements of tangential shear around voids, which provides the projected surface-mass density excess between weakly lensed source galaxies and the observer. Shape catalogues of the galaxies in DES are available, a study of the absolute tracer bias with respect to the underlying dark matter distribution in void environments is underway (Fang et al., in prep.). Our conclusions are further in excellent agreement with recent analyses of weak lensing by troughs in the projected galaxy distribution (Gruen et al. 2016, 2017), which can be accurately modelled using linear bias (Friedrich et al. 2017). While those results argue for a non-vanishing stochasticity parameter to be important for the counts-in-cells statistic, this does not apply to cross-correlation functions (as employed in this paper), where stochasticity does not enter at non-zero separation.

As a side product, we have constructed the first catalogue of 3D-watershed voids that are solely based on photometric redshift measurements with a controlled photo-z uncertainty.[7] Another element of novelty in our approach is that we employ galaxy clusters, rather than single galaxies, as tracers for void finding. In fact, our tests with mocks indicate that while the accuracy of REDMAGIC redshift estimates for single galaxies is not sufficient to match void number counts from a spectroscopic survey, REDMAPPER clusters produce remarkably similar void abundances among spec-z and photo-z catalogues. The flip side of using clusters rather than galaxies as void tracers is that they can only access fewer and larger voids, due to their sparsity. Nevertheless, for our purposes this constitutes also an advantage, as the relative impact of photo-z scatter becomes even smaller for large voids. Furthermore, the high number of clusters accessible in photometric surveys opens up a promising perspective for void science in the future. In fact forthcoming surveys, such as LSST (Ivezic et al. 2008) and EUCLID (Laureijs et al. 2011), will partially rely on photometric redshift estimates. The effort to fully exploit these kind of data in the context of void studies will thereby benefit from our analysis.

---

[7] Granett et al. (2008) have already extracted a 3D void catalogue from SDSS photometry, but analysed it in projection to study ISW imprints.

REFERENCES

Abbas U., Sheth R. K., 2007, MNRAS, 378, 641
Abbott T. M. C., et al., 2018, preprint, (arXiv:1801.03181)
Achitouv I., 2017, Phys. Rev. D, 96, 083506
Achitouv I., Blake C., Carter P., Koda J., Beutler F., 2017, Phys. Rev. D, 95, 083502
Alcock C., Paczynski B., 1979, Nature, 281, 358
Baldauf T., Seljak U., Smith R. E., Hamaus N., Desjacques V., 2013, Phys. Rev. D, 88, 083507
Baldi M., Villaescusa-Navarro F., 2016, ArXiv e-prints 1608.08057

Barreira A., Cautun M., Li B., Baugh C. M., Pascoli S., 2015, J. Cosmology Astropart. Phys., 8, 28
Bertschinger E., 1985, ApJS, 58, 1
Blas D., Lesgourgues J., Tram T., 2011, J. Cosmology Astropart. Phys., 7, 034
Bocquet S., Saro A., Dolag K., Mohr J. J., 2016, MNRAS, 456, 2361
Cacciato M., Lahav O., van den Bosch F. C., Hoekstra H., Dekel A., 2012, MNRAS, 426, 566
Cai Y.-C., Neyrinck M. C., Szapudi I., Cole S., Frenk C. S., 2014, ApJ, 786, 110
Cai Y.-C., Taylor A., Peacock J. A., Padilla N., 2016, MNRAS, 462, 2465
Cautun M., Paillas E., Cai Y.-C., Bose S., Armijo J., Li B., Padilla N., 2017, preprint, (arXiv:1710.01730)
Ceccarelli L., Paz D., Lares M., Padilla N., Lambas D. G., 2013, MNRAS, 434, 1435
Chan K. C., Hamaus N., Desjacques V., 2014, Phys. Rev. D, 90, 103521
Chon G., Challinor A., Prunet S., Hivon E., Szapudi I., 2004, MNRAS, 350, 914
Chuang C.-H., Kitaura F.-S., Liang Y., Font-Ribera A., Zhao C., McDonald P., Tao C., 2017, Phys. Rev. D, 95, 063528
Clampitt J., Jain B., 2015, MNRAS, 454, 3357
Clampitt J., Cai Y.-C., Li B., 2013, MNRAS, 431, 749
Clampitt J., Jain B., Sánchez C., 2016, MNRAS, 456, 4425
Colberg J. M., Sheth R. K., Diaferio A., Gao L., Yoshida N., 2005, MNRAS, 360, 216
Crocce M., Castander F. J., Gaztañaga E., Fosalba P., Carretero J., 2015, MNRAS, 453, 1513
DES Collaboration et al., 2017, preprint, (arXiv:1708.01530)
DESI Collaboration et al., 2016, preprint, (arXiv:1611.00036)
Davis M., Peebles P. J. E., 1983, ApJ, 267, 465
Desjacques V., Jeong D., Schmidt F., 2016, preprint, (arXiv:1611.09787)
Di Dio E., Montanari F., Lesgourgues J., Durrer R., 2013, J. Cosmology Astropart. Phys., 11, 044
Dolag K., Vazza F., Brunetti G., Tormen G., 2005, MNRAS, 364, 753
Dolag K., Borgani S., Murante G., Springel V., 2009, MNRAS, 399, 497
Dolag K., Gaensler B. M., Beck A. M., Beck M. C., 2015, Mon. Not. Roy. Astron. Soc., 451, 4277
Dolag K., Komatsu E., Sunyaev R., 2016, MNRAS,
Drlica-Wagner A., et al., 2018, ApJS, 235, 33
Dvornik A., et al., 2018, preprint, (arXiv:1802.00734)
Eke V. R., Cole S., Frenk C. S., 1996, MNRAS, 282
Elvin-Poole J., et al., 2017, preprint, (arXiv:1708.01536)
Falck B., Neyrinck M. C., 2015, MNRAS, 450, 3239
Finelli F., García-Bellido J., Kovács A., Paci F., Szapudi I., 2014, in IAU Symposium. pp 153–155, doi:10.1017/S1743921314013714
Flaugher B., et al., 2015, AJ, 150, 150
Fosalba P., Crocce M., Gaztañaga E., Castander F. J., 2015, MNRAS, 448, 2987
Friedrich O., et al., 2017, preprint, (arXiv:1710.05162)
Granett B. R., Neyrinck M. C., Szapudi I., 2008, ApJ, 683, L99
Gregory S. A., Thompson L. A., Tifft W. G., 1978, in Bulletin of the American Astronomical Society. p. 622
Gruen D., et al., 2016, MNRAS, 455, 3367
Gruen D., et al., 2017, preprint, (arXiv:1710.05045)
Hamaus N., Seljak U., Desjacques V., Smith R. E., Baldauf T., 2010, Phys. Rev. D, 82, 043515
Hamaus N., Sutter P. M., Lavaux G., Wandelt B. D., 2014a, J. Cosmology Astropart. Phys., 12, 013
Hamaus N., Wandelt B. D., Sutter P. M., Lavaux G., Warren M. S., 2014b, Physical Review Letters, 112, 041304
Hamaus N., Sutter P. M., Wandelt B. D., 2014c, Physical Review Letters, 112, 251302
Hamaus N., Sutter P. M., Lavaux G., Wandelt B. D., 2015, J. Cosmology Astropart. Phys., 11, 036
Hamaus N., Pisani A., Sutter P. M., Lavaux G., Escoffier S., Wandelt B. D., Weller J., 2016, Physical Review Letters, 117, 091302

Hamaus N., Cousinou M.-C., Pisani A., Aubert M., Escoffier S., Weller J., 2017, J. Cosmology Astropart. Phys., 7, 014

Hausman M. A., Olson D. W., Roth B. D., 1983, ApJ, 270, 351

Hawken A. J., et al., 2017, A&A, 607, A54

Hirschmann M., Dolag K., Saro A., Bachmann L., Borgani S., Burkert A., 2014, MNRAS, 442, 2304

Honscheid K., DePoy D. L., for the DES Collaboration 2008, preprint, (arXiv:0810.3600)

Ivezic Z., et al., 2008, preprint, (arXiv:0805.2366)

Jennings E., Li Y., Hu W., 2013, MNRAS, 434, 2167

Kaiser N., 1984, ApJ, 284, L9

Kessler R., et al., 2015, AJ, 150, 172

Kirshner R. P., Oemler Jr. A., Schechter P. L., Shectman S. A., 1981, ApJ, 248, L57

Komatsu E., et al., 2011, ApJS, 192, 18

Kovács A., 2018, MNRAS, 475, 1777

Kovács A., et al., 2017, MNRAS, 465, 4166

Kovač K., et al., 2014, MNRAS, 438, 717

Krause E., Chang T.-C., Doré O., Umetsu K., 2013, ApJ, 762, L20

Landy S. D., Szalay A. S., 1993, ApJ, 412, 64

Laureijs R., et al., 2011, preprint, (arXiv:1110.3193)

Lavaux G., Wandelt B. D., 2012, in American Astronomical Society Meeting Abstracts #219. p. 336.02

Li B., 2011, Mon.Not.Roy.Astron.Soc., 411, 2615

Mao Q., et al., 2017, ApJ, 835, 161

Massara E., Villaescusa-Navarro F., Viel M., Sutter P. M., 2015, J. Cosmology Astropart. Phys., 11, 018

McClintock T., et al., 2018, preprint, (arXiv:1805.00039)

McDonald M., et al., 2014, ApJ, 794, 67

Melchior P., Sutter P. M., Sheldon E. S., Krause E., Wandelt B. D., 2014, MNRAS, 440, 2922

Nadathur S., 2016, Monthly Notices of the Royal Astronomical Society, 461, 358

Nadathur S., Crittenden R., 2016, ApJ, 830, L19

Nadathur S., Hotchkiss S., 2015, MNRAS, 454, 2228

Nadathur S., Percival W. J., 2017, preprint, (arXiv:1712.07575)

Nadathur S., Lavinto M., Hotchkiss S., Räsänen S., 2014, Phys. Rev. D, 90, 103510

Neyrinck M. C., 2008, MNRAS, 386, 2101

Neyrinck M. C., Aragón-Calvo M. A., Jeong D., Wang X., 2014, MNRAS, 441, 646

Padilla N. D., Ceccarelli L., Lambas D. G., 2005, MNRAS, 363, 977

Paech K., Hamaus N., Hoyle B., Costanzi M., Giannantonio T., Hagstotz S., Sauerwein G., Weller J., 2017, MNRAS, 470, 2566

Pan D. C., Vogeley M. S., Hoyle F., Choi Y.-Y., Park C., 2012, MNRAS, 421, 926

Paranjape A., Hahn O., Sheth R. K., 2017, preprint, (arXiv:1706.09906)

Peebles P. J. E., 1980, The large-scale structure of the universe

Pisani A., Sutter P. M., Hamaus N., Alizadeh E., Biswas R., Wandelt B. D., Hirata C. M., 2015, Phys. Rev. D, 92, 083531

Planck Collaboration et al., 2013, A&A, 550, A131

Planck Collaboration et al., 2014, A&A, 571, A16

Platen E., van de Weygaert R., Jones B. J. T., 2007, MNRAS, 380, 551

Pollina G., Baldi M., Marulli F., Moscardini L., 2016, MNRAS, 455, 3075

Pollina G., Hamaus N., Dolag K., Weller J., Baldi M., Moscardini L., 2017, MNRAS, 469, 787

Pujol A., Hoffmann K., Jiménez N., Gaztañaga E., 2017, A&A, 598, A103

Rees M. J., Sciama D. W., Stobbs S. H., 1968, Astrophys. Lett., 2, 243

Remus R.-S., Burkert A., Dolag K., Johansson P. H., Naab T., Oser L., Thomas J., 2013, ApJ, 766, 71

Remus R.-S., Burkert A., Dolag K., 2017, in Gil de Paz A., Knapen J. H., Lee J. C., eds, IAU Symposium Vol. 321, Formation and Evolution of Galaxy Outskirts. pp 84–86 (arXiv:1605.06511), doi:10.1017/S1743921316011534

Ricciardelli E., Quilis V., Planelles S., 2013, MNRAS, 434, 1192

Ricciardelli E., Quilis V., Varela J., 2014, MNRAS, 440, 601

Ronconi T., Marulli F., 2017, A&A, 607, A24

Rozo E., et al., 2009, ApJ, 699, 768

Rozo E., Rykoff E., Koester B., Nord B., Wu H.-Y., Evrard A., Wechsler R., 2011, ApJ, 740, 53

Rozo E., et al., 2016, MNRAS, 461, 1431

Rykoff E. S., et al., 2012, ApJ, 746, 178

Rykoff E. S., et al., 2016, ApJS, 224, 1

Sánchez C., et al., 2017, MNRAS, 465, 746

Sheth R. K., van de Weygaert R., 2004, MNRAS, 350, 517

Shi J., Sheth R. K., 2018, MNRAS, 473, 2486

Simon P., Hilbert S., 2017, preprint, (arXiv:1711.02677)

Smith R. E., Scoccimarro R., Sheth R. K., 2007, Phys. Rev. D, 75, 063512

Springel V., 2005, MNRAS, 364, 1105

Springel V., Hernquist L., 2002, MNRAS, 333, 649

Springel V., White S. D. M., Tormen G., Kauffmann G., 2001, MNRAS, 328, 726

Springel V., et al., 2018, MNRAS, 475, 676

Steinborn L. K., Dolag K., Hirschmann M., Prieto M. A., Remus R.-S., 2015, MNRAS, 448, 1504

Steinborn L. K., Dolag K., Comerford J. M., Hirschmann M., Remus R.-S., Teklu A. F., 2016, MNRAS, 458, 1013

Sutter P. M., Lavaux G., Wandelt B. D., Weinberg D. H., 2012a, ApJ, 761, 44

Sutter P. M., Lavaux G., Wandelt B. D., Weinberg D. H., 2012b, ApJ, 761, 187

Sutter P. M., Lavaux G., Hamaus N., Wandelt B. D., Weinberg D. H., Warren M. S., 2014a, MNRAS, 442, 462

Sutter P. M., Pisani A., Wandelt B. D., Weinberg D. H., 2014b, MNRAS, 443, 2983

Sutter P. M., et al., 2015, Astronomy and Computing, 9, 1

Szapudi I., Prunet S., Pogosyan D., Szalay A. S., Bond J. R., 2001, ApJ, 548, L115

Teklu A. F., Remus R.-S., Dolag K., Beck A. M., Burkert A., Schmidt A. S., Schulze F., Steinborn L. K., 2015, ApJ, 812, 29

The Dark Energy Survey Collaboration 2005, ArXiv Astrophysics e-prints,

Yang X., et al., 2017, ApJ, 848, 60

Zivick P., Sutter P. M., Wandelt B. D., Li B., Lam T. Y., 2015, MNRAS, 451, 4215

APPENDIX A: AFFILIATIONS

[1] *Excellence Cluster Universe, Boltzmannstr. 2, 85748 Garching, Germany*

[2] *Universitäts-Sternwarte, Fakultät für Physik, Ludwig-Maximilians Universität München, Scheinerstr. 1, 81679 München, Germany*

[3] *Max-Planck-Institute for Astrophysics, Karl-Schwarzschild Strasse 1, D-85748 Garching, Germany*

[4] *Max Planck Institute for Extraterrestrial Physics, Giessenbachstrasse, 85748 Garching, Germany*

[5] *Department of Physics and Astronomy, University of Pennsylvania, Philadelphia, PA 19104, USA*

[6] *Institut de Física d'Altes Energies (IFAE), The Barcelona Institute of Science and Technology, Campus UAB, 08193 Bellaterra (Barcelona) Spain*

[7] *Kavli Institute for Particle Astrophysics & Cosmology, P. O. Box 2450, Stanford University, Stanford, CA 94305, USA*

[8] *SLAC National Accelerator Laboratory, Menlo Park, CA 94025, USA*

[9] *Cerro Tololo Inter-American Observatory, National Optical Astronomy Observatory, Casilla 603, La Serena, Chile*

[10] *Fermi National Accelerator Laboratory, P. O. Box 500, Batavia, IL 60510, USA*

[11] *Institute of Cosmology & Gravitation, University of Portsmouth, Portsmouth, PO1 3FX, UK*

[12] *Observatories of the Carnegie Institution of Washington, 813 Santa Barbara St., Pasadena, CA 91101, USA*

[13] *CNRS, UMR 7095, Institut d'Astrophysique de Paris, F-75014, Paris, France*

[14] *Sorbonne Universités, UPMC Univ Paris 06, UMR 7095, Institut d'Astrophysique de Paris, F-75014, Paris, France*

[15] *Department of Physics & Astronomy, University College London, Gower Street, London, WC1E 6BT, UK*

[16] *Laboratório Interinstitucional de e-Astronomia - LIneA, Rua Gal. José Cristino 77, Rio de Janeiro, RJ - 20921-400, Brazil*

[17] *Observatório Nacional, Rua Gal. José Cristino 77, Rio de Janeiro, RJ - 20921-400, Brazil*

[18] *Department of Astronomy, University of Illinois at Urbana-Champaign, 1002 W. Green Street, Urbana, IL 61801, USA*

[19] *National Center for Supercomputing Applications, 1205 West Clark St., Urbana, IL 61801, USA*

[20] *Centro de Investigaciones Energéticas, Medioambientales y Tecnológicas (CIEMAT), Madrid, Spain*

[21] *George P. and Cynthia Woods Mitchell Institute for Fundamental Physics and Astronomy, and Department of Physics and Astronomy, Texas A&M University, College Station, TX 77843, USA*

[22] *Department of Physics, IIT Hyderabad, Kandi, Telangana 502285, India*

[23] *Department of Astronomy, University of Michigan, Ann Arbor, MI 48109, USA*

[24] *Department of Physics, University of Michigan, Ann Arbor, MI 48109, USA*

[25] *Institut d'Estudis Espacials de Catalunya (IEEC), 08193 Barcelona, Spain*

[26] *Institute of Space Sciences (ICE, CSIC), Campus UAB, Carrer de Can Magrans, s/n, 08193 Barcelona, Spain*

[27] *Kavli Institute for Cosmological Physics, University of Chicago, Chicago, IL 60637, USA*

[28] *Instituto de Fisica Teorica UAM/CSIC, Universidad Autonoma de Madrid, 28049 Madrid, Spain*

[29] *Institute of Astronomy, University of Cambridge, Madingley Road, Cambridge CB3 0HA, UK*

[30] *Kavli Institute for Cosmology, University of Cambridge, Madingley Road, Cambridge CB3 0HA, UK*

[31] *Department of Physics, ETH Zurich, Wolfgang-Pauli-Strasse 16, CH-8093 Zurich, Switzerland*

[32] *Santa Cruz Institute for Particle Physics, Santa Cruz, CA 95064, USA*

[33] *Center for Cosmology and Astro-Particle Physics, The Ohio State University, Columbus, OH 43210, USA*

[34] *Department of Physics, The Ohio State University, Columbus, OH 43210, USA*

[35] *Harvard-Smithsonian Center for Astrophysics, Cambridge, MA 02138, USA*

[36] *Australian Astronomical Observatory, North Ryde, NSW 2113, Australia*

[37] *Departamento de Física Matemática, Instituto de Física, Universidade de São Paulo, CP 66318, São Paulo, SP, 05314-970, Brazil*

[38] *Department of Astrophysical Sciences, Princeton University, Peyton Hall, Princeton, NJ 08544, USA*

[39] *Institució Catalana de Recerca i Estudis Avançats, E-08010 Barcelona, Spain*

[40] *Jet Propulsion Laboratory, California Institute of Technology, 4800 Oak Grove Dr., Pasadena, CA 91109, USA*

[41] *Department of Physics and Astronomy, Pevensey Building, University of Sussex, Brighton, BN1 9QH, UK*

[42] *School of Physics and Astronomy, University of Southampton, Southampton, SO17 1BJ, UK*

[43] *Brandeis University, Physics Department, 415 South Street, Waltham MA 02453*

[44] *Instituto de Física Gleb Wataghin, Universidade Estadual de Campinas, 13083-859, Campinas, SP, Brazil*

[45] *Computer Science and Mathematics Division, Oak Ridge National Laboratory, Oak Ridge, TN 37831*